January 2018

FONDAZIONE ENI ENRICO MATTEI

Working Paper

001.2018

Some Financial Implications of Global Warming: an Empirical Assessment

Claudio Morana, Giacomo Sbrana

Climate and Sustainable Innovation
Series Editor: Massimo Tavoni

Some Financial Implications of Global Warming: an Empirical Assessment

By Claudio Morana, Università di Milano Bicocca, CeRP-Collegio Carlo Alberto and Rimini Centre for Economic Analysis
Giacomo Sbrana, NEOMA Business School

Summary

Concurrent with the rapid development of the market for catastrophe (cat) bonds, a steady decline in their risk premia has been observed. Whether the latter trend is consistent with the evolution of natural disasters risk is an open question. Indeed, a large share of outstanding risk capital in the cat bonds market appears to be exposed to some climate change-related risk as, for instance, hurricane risk, which global warming is expected to enhance. This paper addresses the above issue by assessing the global warming evidence, its implications for the natural environment and the drivers of cat bonds risk premia. We find that radiative forcing, i.e. the net insolation absorbed by the Earth, drives the warming trend in temperature anomalies and the trend evolution of natural phenomena, such as ENSO and Atlantic hurricanes, enhancing their disruptive effects. Hence, in the light of the ongoing contributions of human activity to radiative forcing, i.e., greenhouse gases emissions, natural disasters risk appears to be on a raising trend. Yet, the latter does not appear to have been accurately priced in the cat bonds market so far. In fact, while we find that the falling trend in cat bonds multiples is accounted by the expansionary monetary stance pursued by the Fed, we do also find evidence of significant undervaluation of natural disasters risk.

Keywords: Cat Bonds, Risk Premia/Multiples, Temperature Anomalies, Global Warming, Radiative Forcing, ENSO, El Niño, Atlantic Hurricanes, Dynamic Conditional Correlation Model

JEL Classification: G11, G23, C32

A previous version of the paper was presented at the 2016 and 2017 Conference on Econometric Models of Climate Change (Aarhus University; Oxford University). The authors are grateful to conference participants for constructive comments. We are grateful to Steve Evans (Artemis) for allowing the reproduction of Artemis's charts.

Address for correspondence:
Claudio Morana
Università di Milano-Bicocca
Dipartimento di Economia, Metodi Quantitativi e Strategie di Impresa
Piazza dell'Ateneo Nuovo, 1
20126 Milano
Italy
E-mail: claudio.morana@unimib.it

Some financial implications of global warming: An empirical assessment*

Claudio Morana*†, Giacomo Sbrana+

*Università di Milano Bicocca, CeRP-Collegio Carlo Alberto (Moncalieri, Italy)
and Rimini Centre for Economic Analysis (Rimini, Italy).

+NEOMA Business School

December 2017

Abstract

Concurrent with the rapid development of the market for catastrophe (cat) bonds, a steady decline in their risk premia has been observed. Whether the latter trend is consistent with the evolution of natural disasters risk is an open question. Indeed, a large share of outstanding risk capital in the cat bonds market appears to be exposed to some climate change-related risk as, for instance, hurricane risk, which global warming is expected to enhance. This paper addresses the above issue by assessing the global warming evidence, its implications for the natural environment and the drivers of cat bonds risk premia. We find that radiative forcing, i.e. the net insolation absorbed by the Earth, drives the warming trend in temperature anomalies and the trend evolution of natural phenomena, such as ENSO and Atlantic hurricanes, enhancing their disruptive effects. Hence, in the light of the ongoing contributions of human activity to radiative forcing, i.e., greenhouse gases emissions, natural disasters risk appears to be on a raising trend. Yet, the latter does not appear to have been accurately priced in the cat bonds market so far. In fact, while we find that the falling trend in cat bonds multiples is accounted by the expansionary monetary stance pursued by the Fed, we do also find evidence of significant undervaluation of natural disasters risk.

Keywords: Cat bonds, risk premia/multiples, temperature anomalies, global warming, radiative forcing, ENSO, El Niño, Atlantic hurricanes, dynamic conditional correlation model.
JEL classification: G11, G23, C32

*A previous version of the paper was presented at the 2016 and 2017 Conference on Econometric Models of Climate Change (Aarhus University; Oxford University). The authors are grateful to conference participants for constructive comments. We are grateful to Steve Evans (Artemis) for allowing the reproduction of Artemis's charts.

†Address for correspondence: Claudio Morana, Università di Milano-Bicocca, Dipartimento di Economia, Metodi Quantitativi e Strategie di Impresa, Piazza dell'Ateneo Nuovo 1, 20126, Milano, Italy. E-mail: claudio.morana@unimib.it.

1 Introduction

Catastrophe bonds, or cat bonds, are natural disaster risk-linked securities which have the purpose of transferring natural disasters risk from an issuer/insurance company to investors in the bonds markets. By purchasing a cat bond, investors take on the risks of the occurrence of a specified natural disaster against the payment of a return. In the occurrence of the event the investors will then loose the capital invested and the issuer will use that money to cover the damages.[1] Cat bonds were created in the mid-1990s, after hurricane Harvey in 1992 led eleven insurance companies to bankruptcy as a direct or indirect result of the damages inflicted by the storm. Hurricane Andrew served as a wake-up call for the insurance industry, showing that the tail risk associated with natural disasters might be so severe that insurance companies themselves might not have enough reserves to cover it. Insurance securitization was then seen as an effective risk sharing mechanism, to spread natural disaster risk through financial markets and investors.

Since their introduction, the size of the cat bonds market has grown steadily, rising to about US$ 10 billions in the mid-2000s, and then to over US$ 30 billions by the following decade (Figure 1; top plot, LHS). Owner composition of cat bonds has also been changing over time: while in the early 2000s cat bonds were largely owned by hedge funds and reinsurance companies, currently institutional investors, including pension funds and mutual funds, own about 30% of total assets (Figure 1; bottom plot, LHS). These changes have been coupled by a steady decline in return per unity of risk or *multiple*, i.e. the coupon (net of the risk free rate) to the Expected Loss (EL) ratio (Figure 1; top plot, RHS). Cat bond multiples/risk premia have been falling from a value of 8 in 2000 to about 4 in 2003. Since 2012 a new contraction in multiples can be noted, falling to a record low value of 2 in 2017.

Despite the prolonged contraction in cat bond risk premia is a shared feature with more traditional asset classes, such as corporate bonds (Figure 1; center plot, RHS), and possibly related to the response of monetary policy to the recent financial crises[2], it might also reflect a change in investors' perception about cat bonds as portfolio diversification assets, i.e. from an "exotic" to a more standard instrument. In the logic of portfolio risk diversification, cat bonds are, in fact, attractive assets, being not correlated with traditional bond market instruments (Davies, 2017).

Given the increasing participation of institutional investors to the cat bonds market, and the limits to risk exposure imposed by current regulation for pension funds, in particular, an important open question is then whether cat bonds risk is currently correctly perceived and priced. This paper attempts to answer the latter question by investigating whether the falling trend in cat bonds risk premia is consistent with trend dynamics in natural disaster risk, which, due to ongoing climate change, is actually expected to increase. This is also in the light of the large share of outstanding capital in the cat bonds market which is exposed to Atlantic hurricanes (Figure 1; bottom plot, LHS), whose in-

[1] See http://www.artemis.bm/library/what-is-a-catastrophe-bond.html for a quick introduction to cat bonds.

[2] For instance, since 2007 Fed's balance sheet has risen by $3.5 trillion, from $0.9 trillion to $4.4 trillion. Engen et al. (2015) suggest that the effect of the entire QE programme was to reduce the 10-year term premium, and therefore the bond yield, by 120 basis points in 2013. The QE programme also increased US equity prices by 11-15 per cent, and reduced the dollar effective exchange rate by 4.5-5 per cent. Other central banks, such as the Bank of England, the Bank of Japan and the European Central Bank have implemented similar policies. It is then likely that the expansionary monetary policy stance might have also determined a surplus of capital in the reinsurance industry.

tensity might be enhanced by global warming (IPCC, 2012), also through its impact on natural oscillations, such as the El Niño Southern Oscillation (ENSO; Cai et al., 2015a,b; 2014; Kim et al., 2014).[3]

The deep economic and human implications of these facts are clearly shown by recent events. For instance, the 2014-2016 El Niño event contributed to the most (least) active tropical cyclone season on record for the Central Pacific basin (Australian region) and to the formation of some systems outside of the season boundaries within the North Atlantic, Eastern and Southern Pacific basins. Various countries around the world, including Africa, Central America, South-East Asia and Pacific Islands, were affected by below or above-average rainfall and flooding, increased food scarcity and susceptibility to illnesses, forced displacement (UNOCHA, 2016). The severity of 2017 Atlantic hurricanes season also appears to be related to ENSO anomalies.[4] At the time of writing, a preliminary total of over US$ 316.51 billions in damages have been accrued and 464 fatalities can be counted. Season 2017 was indeed a record one under many respects: a part from its extreme intensity, all ten of the season's hurricanes occurred in a row, the greatest number of consecutive hurricanes ever observed in the satellite era.[5] Consistent evidence is also yield by the Loss/Risk ratio for Atlantic hurricanes (Figure 1; center plot, RHS), as measured by the ratio of total damages to accumulated cyclones energy (ACE), showing increasing level and volatility since the early 2000s and record high in 2017.

Hence, cat bonds risk assessment appears to require the investigation of the global warming phenomenon (GW) and of its implications for natural disasters. In this paper, the latter analysis is carried out in an innovative econometric framework, i.e. the semi-parametric dynamic conditional correlation model (SP-DCC) of Morana (2015), which allows for accurate modelling of first and second conditional moments of temperature anomalies. Within this framework, we then assess: 1) whether the current warming trend in temperature anomalies is due to radiative forcing, i.e. the net insolation absorbed by the Earth, and, therefore, whether global warming (GW), at least in part, is of anthropogenic origin (carbon dioxide, methane and aerosols emissions); 2) whether there are any feedback effects of GW on the environment, for instance concerning natural phenomena, such as ENSO (El Niño/La Niña episodes) and Atlantic-hurricanes, and their disruptive effects. In the light of the evidence in 1)-2) we then investigate the long- and short-term drivers of cat bonds multiples, in relation not only to the monetary policy stance and investors' preferences, but also to climate change risk.

To summarize the key results of the study, we find that radiative forcing has been driving the warming trend in temperature anomalies since the 1980s, also accounting for their mid-end 1990s level switch, the 1998-2013 "warming hiatus" and their current raise; we also find that radiative forcing is driving the trend evolution of natural phenomena, such as ENSO and Atlantic hurricanes activity, and might enhance their disruptive effects. Hence, our evidence is supportive of the global warming hypothesis and the existence of feedback effects of global warming for the environment, in terms of higher natural disasters risk (more intense cyclones, draughts and floods).

We also document the GARCH properties of the time-varying volatility of tempera-

[3] See also Coumou and Rahmstorf (2012) and Ng et al. (2015) on these issues.

[4] While an El Niño event was initially predicted to develop in 2017, and expected to lower storm activity in the Atlantic, cool-neutral conditions (La Niña) materialized instead, yielding the opposite effect.

[5] In 2017 there were 16 named storms in total; 4 of them reached the intensity of hurricanes, while other 6 were classified as major hurricanes. Season 2017 was therefore a record high also for the total accumulated cyclone energy (221 10^4kt2) and number of major hurricanes since 2005.

ture anomalies and SOI, a feature neglected in the literature so far. In this respect, a sizable increase in SOI volatility can be noted since the mid-2000s, concurrent with the recent steepening in the radiative forcing trend and raise in global temperature volatility, pointing to more unstable ENSO episodes, possibly also as a consequence of GW.

In the light of current contributions of human activity to radiative forcing, i.e., carbon dioxide, methane and aerosols emissions, natural disasters risk, such as hurricanes (as well as extreme droughts and floods), then appears to be on a raising trend. Similarly on a raising trend is then cat bonds risk, at least with reference to that sizable portion of outstanding capital facing some exposure to climate change-related risk. However, the latter risk dynamics do not appear to have been properly incorporated in cat bonds multiples so far. In fact, while we find that falling cat bonds risk premia should be related to the expansionary monetary stance pursued by the Fed, as well as to some portfolio shift effects, we also find evidence of significant undervaluation of natural disasters risk. As an implication, it appears that cat bonds might not be a suitable diversification instrument for risk-adverse investors, such as pension funds. Moreover, due to risk undervaluation, the overall sanity of the market, as well as whether, in a not too far future, the cat bonds market might become a trigger for a new phase of generalized financial instability, appear to be important issues which do call for assessment a further research.

The rest of the paper is organized as follows. In Section 2 we introduce the data, while in Section 3 we present the econometric model. Then, in Sections 4 and 5 we discuss the empirical results concerning the global warming evidence and risk pricing in the cat bonds market, while Section 6 concludes. In the Appendix we finally report estimation details and Monte Carlo evidence for the SP-DCC estimator. Additional empirical results are contained in the Online Appendix.

2 The data

Our climatological information set is monthly and spans the period 1978:12 through 2016:12, for a total of 457 observations. It consists of average land and ocean temperature anomalies for the entire globe (GL; 90S-90N) and seven zones, namely the Northern Hemisphere (NH; 0-90N), the Southern Hemisphere (SH; 90S-0), the Tropics (Trpcs; 20S-20N), the Northern Extratropic (NoExt; 20N-90N), the Southern Extratropic (SoExt; 90S-20S), the Northern Polar (NoPol; 60N-90N), the Southern Polar (SoPol; 90S-60S). [6] We also include the Southern Oscillation Index (SOI) to track the temporal evolution of ENSO episodes.[7] Moreover, following Hansen et al. (2005), radiative forcing is measured by the sum of various components: Well-Mixed Greenhouse Gases (WMGG; carbon dioxide (CO_2), methane (NH4), nitrous oxide (N2O) and chlorofluorocarbons (CFCs)), Ozone (O3), Stratospheric Water Vapor (StrH2O), Reflective Tropospheric Aerosols (ReflAer), Tropospheric Aerosol Indirect Effects (AIE), Black Carbon Aerosols (BC), Snow Albedo (snowAlb), Stratospheric Aerosols (StrAer), Solar Irradiance (Solar), Land Use

[6] The source is the NASA Goddard Institute for Space Studies and we refer to Christy et al. (2011) for details concerning data construction. The data are available at http://www.nsstc.uah.edu/data/msu/v6.0/tlt/uahncdc_lt_6.0.txt

[7] SOI measures the bimodal variation in sea level barometric pressure between observation stations at Darwin (Australia) and Tahiti. SOI data are available at https://www.ncdc.noaa.gov/teleconnections/enso/indicators/soi/

(including irrigation; LandUse).[8] As radiative forcing data are available at the annual frequency and up to 2011 only, implementation of the monthly model in Sections 4-5 required forecasting radiative forcing data through 2016 and monthly interpolation. Details of the procedure implemented are provided in the Online Appendix. Finally, in order to measure Atlantic cyclones intensity, we consider the accumulated cyclone energy (ACE) index, which is also available annually.[9]

Concerning financial data, due to cat bonds data sample limitations, we consider annual figures for the period 1997 through 2017. In particular, we consider average multiples, the effective federal funds rate, the BofA Merrill Lynch US corporate AA, BBB and BB option-adjusted spreads, US Treasury bills (3-month) and bonds (10-year) rates, and the Loss/Risk ratio for Atlantic hurricanes, as yield by the damages to ACE ratio.[10]

3 The econometric model

The semiparametric dynamic conditional correlation model ($SP-DCC$; Morana, 2015) is defined by the following equations

$$\mathbf{y}_t = \boldsymbol{\mu}_t(\boldsymbol{\delta}) + \boldsymbol{\varepsilon}_t \tag{1}$$

$$\boldsymbol{\varepsilon}_t = \mathbf{H}_t^{1/2}(\boldsymbol{\delta})\mathbf{z}_t \tag{2}$$

where $\mathbf{y}_t = \left[\begin{array}{cccccccc} GL & NH & SH & Trpcs & NoEext & SoExt & NoPol & SoPol & SOI \end{array} \right]'$ is the $N \times 1$ column vector of the variables of interest, i.e. temperature anomalies for various zones and SOI ($N = 9$), $\boldsymbol{\mu}_t(\boldsymbol{\delta})$ is the $N \times 1$ conditional mean vector $E(\mathbf{y}_t|I_{t-1})$, $\boldsymbol{\delta}$ is a vector of parameters, I_{t-1} is the sigma field; $\mathbf{H}_t(\boldsymbol{\delta})$ is the $N \times N$ conditional variance-covariance matrix $Var(\mathbf{y}_t|I_{t-1})$. Moreover, the random vector $\mathbf{z}_t$ is of dimension $N \times 1$ and assumed to be $i.i.d.N$ with first two moments $E(\mathbf{z}_t) = \mathbf{0}$ and $Var(\mathbf{z}_t) = \mathbf{I}_N$.

3.1 The specification of the conditional mean function

We employ an univariate Adaptive-X-ARMA model for each of the N elements in the mean vector $\boldsymbol{\mu}_t(\boldsymbol{\delta})$, i.e.

$$\phi_i(L)\, y_{i,t} = c_{i,t} + \theta_i(L)\, \varepsilon_{i,t} \qquad i = 1, ..., N \tag{3}$$

[8] According to IPCC glossary, radiative forcing or climate forcing is the difference between insolation (sunlight) absorbed by the Earth and energy radiated back to space. Positive (negative) radiative forcing means Earth receives more (less) incoming energy from sunlight than it radiates to space. This net gain (loss) of energy will cause global warming (cooling). Causes of positive radiative forcing include changes in insolation and the concentrations of radiatively active gases, commonly known as greenhouse gases, and aerosols, which (in large part) are the anthropogenic contribution to global warming. RF is measured in W/m2. The data ara available at https://data.giss.nasa.gov/modelforce/Fe_H11_1880-2011.txt

[9] The ACE is calculated by squaring the maximum sustained surface wind in the system every six hours (knots) and summing it up for the season. It is expressed in 10^4kt2. ACE figures can be found at http://www.aoml.noaa.gov/hrd/tcfaq/E11.html.

[10] The source for cat bonds multiples is Artemis (http://www.artemis.bm/deal_directory/cat_bonds_ils_average_multiple.html). Data for the federal funds rate, Treasury bills and bonds, and the AA, BBB, and BB corporate spreads are available from FRED, with acronyms FEDFUNDS, TB3MS, GS10, BAMLC0A2CAA, BAMLC0A4CBBB, and BAMLH0A1HYBB, respectively. Figures for total damages are available season by season on wikipedia; for instance, 2017 figures can be found at https://en.wikipedia.org/wiki/2017_Atlantic_hurricane_season

where $\phi_i(L)$ and $\theta_i(L)$ are polynomials in the lag operator with all the roots outside the unit circle; $c_{i,t}$ is a level component specified according to the general p-order Fourier function in radiative forcing (RF)

$$c_t = c_0 + \sum_{j=1}^{s} c_j I_{j,t} + c_2 RF_t + \sum_{j=1}^{p} \gamma_j \sin(2\pi j RF_t^*) + \sum_{j=1}^{p} \delta_j \cos(2\pi j RF_t^*) \qquad \textbf{MX} \tag{4}$$

where $RF_t^* = \frac{RF_t - \min RF_t}{\max RF_t - \min RF_t}$ is RF_t scaled to range between 0 and 1, and $I_{j,t}$ is a generic step dummy variable with unitary values set according to the Bai and Perron (1998) structural break tests.

We also use the nested specification

$$c_t = c_0 + c_2 RF_t + \sum_{j=1}^{p} \gamma_j \sin(2\pi j RF_t^*) + \sum_{j=1}^{p} \delta_j \cos(2\pi j RF_t^*) \qquad c_2 = 0 \qquad \textbf{MXR}$$

which omits the dummy break variable, and therefore relates the underlying evolution in the series to RF only.

In terms of properties, the Adaptive-X-ARMA model is then consistent with the available evidence in the literature, which suggests the existence of a common trend in temperature anomalies and radiative forcing (Kaufmann et al., 2013; Schmith et al., 2012; Estrada and Perron, 2016), as well as of structural breaks in temperature anomalies, possibly associated with the persistent effects of natural oscillations, such as the El Niño Southern Oscillation (ENSO), the Atlantic Multidecadal Oscillation (AMO) or the Antarctic Oscillation (AAO) (Gay et al., 2009; Mills, 2013, Estrada and Perron, 2016; McKitrick and Vogelsang, 2014).

3.2 The specification of the conditional variance function

Concerning the conditional variance-covariance matrix $\mathbf{H}_t(\boldsymbol{\delta})$, we assume that the elements along its main diagonal, i.e. the conditional variances $Var(y_{i,t}|I_{t-1}) \equiv h_{i,t}$ follow a GARCH(1,1) process

$$h_{i,t} = \omega_i + \alpha_i \varepsilon_{i,t-1}^2 + \beta_i h_{i,t-1} \qquad i = 1, ..., N \tag{5}$$

subject to the usual restrictions to ensure that the conditional variances are positive almost surely at any point in time.

Concerning the definition of the off-diagonal elements of $\mathbf{H}_t$, i.e. the conditional covariances $Cov(y_{i,t}, y_{j,t}|I_{t-1}) \equiv h_{ij,t}$, the latter are defined according to the *polarization* identity of the covariance operator[11]

$$h_{ij,t} = \frac{1}{4}\left[Var_{t-1}(y_{i,t} + y_{j,t}) - Var_{t-1}(y_{i,t} - y_{j,t})\right] \qquad i, j = 1, ..., N \qquad i \neq j. \tag{6}$$

By defining the aggregate variables $y_{ij,t}^+ \equiv y_{i,t} + y_{j,t}$ and $y_{ij,t}^- \equiv y_{i,t} - y_{j,t}$, and assuming a GARCH(1,1) specification for their conditional variance processes $Var_{t-1}(y_{ij,t}^+|I_{t-1}) \equiv h_{ij,t}^+$ and $Var_{t-1}(y_{ij,t}^-|I_{t-1}) \equiv h_{ij,t}^-$, one then has

$$h_{ij,t} = \frac{1}{4}\left[h_{ij,t}^+ - h_{ij,t}^-\right] \qquad i, j = 1, ..., N \qquad i \neq j \tag{7}$$

[11] For any two random variables A and B, one has $Cov(A, B) \equiv \frac{1}{4}\left[Var(A + B) - Var(A - B)\right]$, since $Var(A \pm B) = Var(A) + Var(B) \pm 2Cov(A, B)$.

where

$$h^{+}_{ij,t} = \omega^{+}_{ij} + \alpha^{+}_{ij}\varepsilon^{+2}_{ij,t-1} + \beta^{+}_{ij}h^{+}_{ij,t-1} \qquad i,j = 1,...,N \qquad i \neq j \tag{8}$$

$$h^{-}_{ij,t} = \omega^{-}_{ij} + \alpha^{-}_{ij}\varepsilon^{-2}_{ij,t-1} + \beta^{-}_{ij}h^{-}_{ij,t-1} \qquad i,j = 1,...,N \qquad i \neq j \tag{9}$$

with $\varepsilon^{+}_{ij,t} = \varepsilon_{i,t} + \varepsilon_{j,t}$ and $\varepsilon^{-}_{ij,t} = \varepsilon_{i,t} - \varepsilon_{j,t}$.

3.3 Estimation of the SP-DCC model

Starting with the Gaussian log-likelihood for the model in (1)-(2)

$$L = -\frac{1}{2}\sum_{t=1}^{T}\left(N\log(2\pi) + \log|\mathbf{H}_t| + \boldsymbol{\varepsilon}_t'\mathbf{H}_t^{-1}\boldsymbol{\varepsilon}_t\right), \tag{10}$$

consistent and asymptotically Normal estimation is obtained by QML, following a multi-step procedure. Firstly, the mean equation model in (1) is estimated equation by equation by QML, i.e. the misspecified likelihood

$$L_m(\boldsymbol{\vartheta}) = -\frac{1}{2}\sum_{t=1}^{T}\sum_{i=1}^{N}\log(2\pi) + \log\sigma_i^2 + \frac{\varepsilon_{i,t}^2}{\sigma_i^2} \tag{11}$$

is maximized by separately maximizing each term.

Then, using the estimated conditional mean residuals $\hat{\boldsymbol{\varepsilon}}_t$, the conditional variance model is estimated by QML using the misspecified GARCH likelihood

$$L_v(\boldsymbol{\theta}) = -\frac{1}{2}\sum_{t=1}^{T}\sum_{i=1}^{N}\log(2\pi) + \log h_{i,t} + \frac{\hat{\varepsilon}_{i,t}^2}{h_{i,t}}, \tag{12}$$

which is jointly maximized by separately maximizing each term.

Similarly for the aggregate series $y^{+}_{ij,t}$ and $y^{-}_{ij,t}$, i.e. the GARCH likelihood

$$\begin{aligned} L_{SP}(\boldsymbol{\phi}) \;=\; & -\sum_{t=1}^{T}\sum_{i=1}^{N}\sum_{j>i}^{N}\left(\log(2\pi) + \log h^{+}_{ij,t} + \frac{\hat{\varepsilon}^{+2}_{ij,t}}{h^{+}_{ij,t}}\right) \\ & -\sum_{t=1}^{T}\sum_{i=1}^{N}\sum_{j>i}^{N}\left(\log(2\pi) + \log h^{-}_{ij,t} + \frac{\hat{\varepsilon}^{-2}_{ij,t}}{h^{-}_{ij,t}}\right) \end{aligned} \tag{13}$$

with $\hat{\varepsilon}^{+}_{ij,t} = \hat{\varepsilon}_{i,t} + \hat{\varepsilon}_{j,t}$ and $\hat{\varepsilon}^{-}_{ij,t} = \hat{\varepsilon}_{i,t} - \hat{\varepsilon}_{j,t}$, is jointly maximized by separately maximizing each term.

The conditional covariances are then estimated by means of the polarization identity, i.e. the off-diagonal elements of $\mathbf{H}_t$, $h_{ij,t}$, $i,j = 1,...,N$, $i \neq j$, are computed as

$$\hat{h}_{ij,t} = \frac{1}{4}\left[\hat{h}^{+}_{ij,t} - \hat{h}^{-}_{ij,t}\right] \qquad i,j = 1,...,N \qquad i \neq j. \tag{14}$$

The conditional correlation matrix $\mathbf{R}_t$ is finally estimated as

$$\hat{\mathbf{R}}_t = \hat{\mathbf{D}}_t^{-1}\hat{\mathbf{H}}_t\hat{\mathbf{D}}_t^{-1} \tag{15}$$

where $\hat{\mathbf{D}}_t = diag\left(\hat{h}_{1,t}^{1/2},...,\hat{h}_{N,t}^{1/2}\right)$. See the Appendix for further details and Monte Carlo results.

4 Empirical results

QML estimates of the models are reported in Table 1, Panel A (MX) and Panel B (MXR). Concerning the specification of the break dummies for the MX model, as shown in the Online Appendix (Table 2, Panel C), the $UD - max$ test points to a single break point over the investigated sample. Consistent with McKitrick and Vogelsang (2014), the break would be located about the mid-/end 1990s (1995 through 1998), and might therefore be related to the concurrent El Niño events (weak: 1995-1996; very strong: 1997-1998) and fading away of the cooling effect of the vulcanian eruption in the Philippines (Mt. Pinatubo in 1991).

As shown in Table 1, all models are equivalent in terms of residual properties as in none of the cases evidence of misspecification is detected by standard diagnostics. Moreover, according to the coefficient of determination, the explanatory power of the various models is similarly sizable, i.e. about 0.70 for GL, NH and SH and 0.80 for Trpcs; low for the Poles, i.e. 0.30 and 0.10 for NoPol and SoPol, respectively; intermediate, i.e. 0.40 to 0.60, for NoExt, SoExt and SOI.

The weaker connection of the trend component for Trpcs with radiative forcing is consistent with the potential effects of extreme ENSO episodes, such as in 1997-1998 and 2015-2016, which might have yield a sizable and long lasting impact on average temperatures, particularly at the tropics. As pointed out by Cai et al. (2015a,b; 2014) and Kim et al. (2014), extreme ENSO events are different from moderate events and, in assessing the evidence on global warming (GW), the latter should be kept separate from normal episodes.[12] The stronger persistence of Trpcs relative to the other anomalies, as well as the different autoregressive structure, might indeed be related to the occurrence of extreme ENSO episodes, which might impart an upward bias to the estimated autoregressive parameter.[13]

In the light of the above assessment we have then selected the Adaptive-X-AR model (MXR, Panel B) as best model. As shown in the plots in Figure 2, the radiative forcing nonlinear trend closely tracks the low frequency evolution in temperature anomalies, accounting not only for their recent raise and mid-end 1990s level switch, but also for the 1998-2013 warming hiatus (slowdown in GW). This is consistent with Estrada and Perron (2016), who relate the hiatus to radiative forcing, i.e. to CFC and methane reductions, rather than to natural variability factors such as AMO, PDO, ENSO, or lower solar activity. See also Kosaka and Xie (2013) and Pretis et al. (2015) on this issue. Therefore, our results appear to be supportive of the "GW hypothesis".

Our results have also implications for the recent debate concerning the effects of GW on the frequency and amplitude of the ENSO phenomenon. The statistical significance of the radiative forcing variable in the SOI conditional mean specification points in fact to a

[12] In this respect, Jones (1989) and Wigley (2000) find that following a typical El Niño event the global surface air temperature increases of up 0.1 C with a lag of 6 months. A larger impact of 0.2 C is documented by Christy and McNider (1994) and Angell (2000) in correspondence of the 1997-1998 very strong El Niño event.

[13] The consensus view on the contribution of ENSO to GW indeed posits that ENSO might account for between 10% and 30% of the inter seasonal and longer-term change in surface and/or lower tropospheric temperature, but little of the global mean warming trend since the 1950s (Foster et al., 2009). The latter warming trend is generally related to RF (Kaufmann et al., 2013; Schmith et al., 2012; Estrada and Perron, 2016). Yet, Douglas and Christy (2009) show that about 88% of the temperature anomaly over the period 1979-2007 might be accounted by ENSO (El Niño3.4 lagged 4 months) and volcano climate forcing. A connection between the North Atlantic Oscillation (NAO), the Arctic Oscillation (AO) and global warming has also bee investigated. See Cohen and Barlow (2005).

feedback effect from global warming to ENSO. This is consistent with the view that ENSO and other natural oscillations might increase in amplitude and frequency and that their teleconnections might be shifted, both as consequences of mean climate state changes (Cai et al.. 2015a,b; 2014; Kim et al., 2014; Ng et al., 2015; Coumou and Rahmstorf, 2012). Our findings are supportive of the above arguments, since the negative sign of the estimated coefficient of the RF variable (γ_4) implies that global warming (cooling) enhances El Niño (La Niña) events. Interestingly, the linkage between RF and ENSO appears to be highly nonlinear and similar to what detected for Trpcs, the geographical zone which is most closely and directly affected by ENSO.

4.1 Robustness check

In order to check the robustness of our conclusions to data extension and interpolation, models MX and MXR were firstly reestimated over the shorter sample 1978:12 through 2011:12, therefore omitting the forecasted RF data; moreover, the model were reestimated over the full sample, yet using the raw step function data, rather than their smoothed values. The results are reported in Tables A4 and A5 in the Online Appendix. By comparing figures reported in Tables 1 and A4, it can then be noticed that the results are strongly robust to the use of forecasted data, since omitting the last five years of (forecasted) data leaves even point estimates virtually unchanged. Moreover, by comparing the estimates reported in Tables 1 and A5, it can be concluded that the sign and magnitude of the contribution of RF to the determination of temperature anomalies is again virtually unchanged, albeit some differences in the order or type of the selected trigonometric components can be noted in few cases. However, in only in three out of eighteen cases the models estimated using step function data are preferred, according to information criteria, to the models estimated using the smoothed interpolated data (GL and NoExt for MX; Trpcs for MXR). Further support for the empirical analysis is provided by the model selection exercise reported in the Online Appendix, showing that the MX and MXR models are superior to a comprehensive set of competing specifications neglecting the contribution of RF.

4.2 The conditional variance of anomalies

The estimated conditional standard deviations for temperature anomalies and SOI are plotted in Figure 3. As shown in the plots, all anomaly series show clusters of more and less sizable changes alternating over time. The latter GARCH feature suggests that temperature risk (or volatility) is not only time-varying, but that abnormal/extreme temperature changes occur in clusters. This property has important implications concerning temperature forecasting in general, and for the pricing of financial instruments traded to hedge against temperature risk. In this respect, GL volatility has been raising since the 1980s and stabilized at a high level during the "hiatus"; a new phase of raising volatility seems to have started since 2010. Interesting patterns can also be detected for the other zones; for instance, temperature volatility appears to be on a upward trend for NH and NoExt and on a downward trend for SH and SoExt. Also noteworthy is the volatility spike in Trpcs, concurrent with the extreme 1997-1998 El Niño event. We are unaware of previous contributions to the literature pointing to GARCH properties of temperature anomalies.

Moreover, the GARCH property can also be detected for SOI. As shown in Figure 3,

a sizable increase in SOI volatility can be noted since the early 2000s, therefore pointing to more "unstable ENSO" over time. The latter finding is interesting and surely deserves further study, particularly in connection with the concurrent steepening in the radiative forcing trend shown in Figure 3, and therefore with potential feedback effects of GW.

4.3 Conditional correlations and global warming

Estimation of the conditional covariances and correlations is performed by means of the polarization identity in (14), which requires the estimation of the conditional variance for the aggregate anomaly and SOI series $y^+_{ij,t}$ and $y^-_{ij,t}$, i.e. $\hat{h}^+_{ij,t}$ and $\hat{h}^-_{ij,t}$, using the corresponding aggregated residuals $\hat{\varepsilon}^+_{ij,t}$ and $\hat{\varepsilon}^-_{ij,t}$.

As for the 9 original series, an IGARCH(1,1) specification is selected also for any of the 72 aggregate cases, with the same estimated persistence parameter, equal to 0.99 (not reported). A summary of the results is provided in Figure 4, where Boxplots for the p-value of the Box-Ljung tests for serial correlation and conditional heteroskedasticity are plotted for the 81 standardized residual series. As shown in the plots, the models are well specified in all cases, since standardized residuals behave according to a white noise process. Given the single decay factor IGARCH (1,1) specification, positive definiteness at each point in time of the conditional variance-covariance and correlation matrices is granted.

Support for the modeling of time-varying conditional correlations across temperature series and SOI is also provided by the comparison with the Constant Conditional Correlation model of Bollerslev (1990; CCC). $SP-DCC$ is in fact preferred to CCC, yielding a lower BIC information criterion, i.e. -9.5651 versus -9.2682 (not reported). $SP-DCC$ is also preferred to Engle (2002) DCC (BIC = -9.3973; not reported).[14] The latter finding is fully consistent with the results of the Monte Carlo analysis reported in the Appendix, showing that $SP-DCC$ outperforms Engle (2002) DCC in the IGARCH(1,1) framework.

In Figure 5 we plot the conditional correlations for non overlapping zones in the Northern and Southern hemispheres, i.e. NH/SH, NoExt/SoExt, NoPol/SoPol. An upward sloping trend can be detected in all cases, revealing increasing comovement of temperature anomalies over time. We interpret the latter finding as further evidence in support of the GW hypothesis, since it suggests the existence of a common driver of the warming trend in temperature anomalies, i.e., RF. Additional results, concerning the ENSO teleconnection and its evolving properties, are reported in the Online Appendix.

4.4 Implications of global warming for natural disasters risk

Conditional mean and variance modelling of temperature anomalies and SOI allow to draw some important conclusions concerning climate change risk. Firstly, we find evidence of ongoing GW. In fact, the warming trend in temperature anomalies appears to be determined by RF; coherently, also an increasing positive correlation or comovement of anomalies across non-overlapping geographical zones is detected. Secondly, we find that GW might exercise feedback effects on the environment, by enhancing the intensity of ENSO events. In fact, RF also appears to drive trend fluctuations in SOI. Thirdly, we find evidence of time varying temperature and SOI volatility. In particular, GL volatility shows a rapid increase since the mid-1980s, stabilizing at much higher levels during the "hiatus"; a new phase of raising GL volatility seems to have started since 2010. Moreover,

[14] Details are available upon request from the authors.

an increase in SOI volatility can be noted since the early 2000s. Hence, given current contributions of human activity to radiative forcing, i.e. current carbon dioxide, methane and aerosol emission levels, more intense and unstable ENSO events and a higher risk of associated disruptive phenomena, i.e. cyclones, floods and droughts, should be expected. In this respect, the economic and human implications of the 2014-2016 El Niño event, as well as of the hyperactive 2017 Atlantic hurricanes season, are the most recent evidence consistent with this view.

In this Section we further assess the predictability of climate-change related disasters. In particular, since about half of the current US$ 30 billions of outstanding risk capital in the cat bonds market might be facing some exposure to Atlantic hurricane risk, we investigate the linkage between radiative forcing, i.e. the GW driver, and Atlantic hurricanes intensity, as measured by its accumulated cyclones energy (ACE). As shown in Figure 6, over the last thirty years, Atlantic hurricanes activity has undergone some noteworthy changes. In fact, since the mid-1990s Atlantic storms intensity appears to have raised to very high levels, particularly during five episodes, i.e. 1995, 1998-1999, 2003-2005, 2010 and 2016-2017 (top plot, shaded areas). The increase in level (and volatility) is concurrent with the level switch detected in temperature anomalies, and related to RF dynamics. Indeed, as shown in the plot, RF does appear to well track also ACE trend developments, and might therefore be a useful conditioning variable in an econometric model for hurricanes risk.

4.4.1 An econometric model of hurricanes risk

Our econometric analysis of hurricanes risk is based on the following parsimonious reduced form Adaptive-X-AR model

$$\begin{aligned} \phi(L)ACE_t &= \gamma(L)RF_t + \sum\nolimits_{i=1}^{p} \theta(L)\sin\left(2\pi i RF_t^*\right) + \delta(L)h_{GL,t}^{1/2} + \varepsilon_t \\ \varepsilon_t &\sim i.i.d.N(0,\sigma^2) \end{aligned} \tag{16}$$

where $\phi(L)$, $\gamma(L)$, $\theta(L)$ and $\delta(L)$ are polynomials in the lag operator with all the roots outside the unit circle, RF (RF^*) is radiative forcing (normalized to range in the $[0,1]$ interval), $h_{GL}^{1/2}$ is the annualized volatility of the global temperature anomaly delivered by the monthly econometric model[15]. For numerical convenience all the variables are reported in standardized units.

Model selection has been implemented following a general to specific reduction approach, allowing for up to five lags of each variables.[16] The selected econometric model is reported in Table 2, Panel A. In addition to the Adaptive-X-AR model, we also report two nested specifications, i.e. the AR model, which neglects past climatological information ($\gamma(L) = \theta(L) = \delta(L) = 0$), and the Adaptive-X model, which neglects past ACE information ($\phi(L) = 1$). According to residuals diagnostics, all the models appear to be well specified. The adaptive models are however clearly preferred to the AR model in terms of fit and information criteria: the coefficient of determination is 0.71 for the Adaptive-X-AR model and 0.59 for the Adaptive-X model; only 0.07 for the AR model. See also Figure 6 (second plot from above).

[15] It is computed as $\left(\sum_{i=1}^{12} h_{GLi,t}\right)^{1/2}$ $t = 1979, ...2016$.

[16] We also considered other potential conditioning variables, as for instance SOI level and volatility. However, the preferred econometric model did not include the latter variables.

From the solved long-run equation (Table 2, Panel A), it can be noticed that an increase in both radiative forcing and temperature volatility would lead to a long-term increase in ACE, and therefore in Atlantic hurricane risk. Hence, Atlantic hurricanes intensity/risk would be enhanced by global warming, also consistent with the feedback effects of GW on ENSO. As found for temperature anomalies and ENSO, given the significance of the trigonometric term, also the linkage between RF on ACE appears to be highly nonlinear.

As shown in Table 2, Panel B, the noteworthy in sample performance of the Adaptive-X-AR and Adaptive-X models is genuine not due to overfitting; both models in fact largely dominate the AR model also in terms of out of sample forecasting accuracy. We have considered two types of forecasting exercises, using 2/3 of the sample for estimation (1984-2006) and 1/3 for forecasting (2007-2017); in the first exercise parameters are estimated over the period 1984-2006 and then one-step ahead forecasts are generated over the period 2007 trough 2017 (without re-estimating the parameters); in the second exercise, one-step ahead forecasts are generated over the period 2007 trough 2017, updating at each step parameter estimates; for both cases, we also report results when the last observation in the sample, i.e. 2017, is omitted from the forecasting horizon, due to its outlying behavior. As shown in the Table, results are robust to the type of exercise undertaken, pointing to 40% and 50% reductions in $RMSFE$ yield by the adaptive models relative to the AR and random walk/naive forecasting models, respectively. The forecasting performance of the adaptive models is similar, with the Adaptive-X-AR model slightly outperforming the Adaptive-X model when forecasts are generated recursively.

In Figure 6 (second plot from below and bottom plot) we compare actual ACE values with the forecasted figures obtained from the Adaptive-X-AR model, for the case of recursive estimation. In the comparison we also consider (spline) smoothed ACE figures in order to highlight the ability of the Adaptive-X-AR model to track trend developments in ACE, consistent with the view that RF/GW might also affect the long-term behavior of natural phenomena. Visual inspection provides clear-cut confirmation of the statistical evidence of predictability of trend Atlantic hurricanes intensity (and disruptions), based on climatological information. Hence, in the light of current climatic developments, the risk of natural disruptions stemming from GW, as for instance extremely severe hurricanes, appears to be on a raising trend. Then, on a raising trend would also be cat bonds risk, at least for that (very sizable) portion of outstanding capital facing some exposure to climate change and GW. This is also consistent with the raising trend and volatility shown by the Atlantic hurricanes Loss/Risk ratio, and its record high in 2017 (Figure 1; bottom plot, RHS). Whether the falling trend in average cat bond risk premia and their record low value scored in 2017 are consistent with accurate pricing of natural disasters risk is then an open issue, which we address in the following Section.

5 Assessing risk premia in the cat bonds market

As shown in Figure 1 (bottom plot, RHS), falling risk premia are a feature shared also with more standard bond classes, as for instance corporate bonds. In the literature, the latter pattern is often associated with the expansionary monetary policy stance pursued by the Fed to counteract the deflationary effects of the dot-com and subprime financial crises, and therefore to the falling trend in the federal funds rate (FFR) and the $Q.E.$ policy.

However, coherent with the different risk exposure, trend dynamics in cat bond multiples ($MULT$) and corporate rate spreads also show some differences. For instance, multiples have been much less affected by the subprime financial crisis. Indeed, the comovement between AA and BBB corporate bond spreads (AA, BB) is much stronger than between AA or BB spreads and multiples. In addition to monetary policy, changes in investors' perception about the characteristics of cat bonds, i.e. from exotic to standard diversification instruments, might then have also contributed to the observed contraction in multiples.

In the light of the nonstationarity properties of multiples and corporate spreads (Table 3, Panel A), we have then first assessed their cointegration properties and then estimated an error correction model to investigate risk premia short-run dynamics. As shown in Table 3 (Panel A), concerning the specification of the unrestricted reduced form model, a parsimonious first order VAR model yields residuals consistent with white noise properties (not reported).[17] Within this framework, we have then tested for cointegration using the Johansen Trace test. According to the Trace statistics there is evidence of two cointegrating relationships (10% significance level) and therefore of two common trends accounting for the long-term evolution of risk premia and the federal funds rate. The identification of the cointegrating vectors yields two irreducible homogenous cointegration relationships: the former relates multiples to the federal funds rate; the latter relates the AA and BBB spreads.[18]

Also consistent and clear-cut are the error correction properties of the spreads. In fact, according to the estimated loadings, multiples correct their disequilibrium with FFR, which, on the other hand, is weakly exogenous. Moreover, also corporate spreads correct relative to the MULT/FFR disequilibrium. Hence, following a contraction in FFR, and therefore a widening in the MULT/FFR disequilibrium ceteris paribus, multiples and corporate spreads would tend to decrease, consistent with the view that associates the declining trend in bond spreads to expansionary monetary policy.

Moreover, the AA spread corrects also relative to its disequilibrium with the BBB spread, pointing to some contagion in the corporate bonds market. In particular, following an increase in the BBB spread, and therefore in the default risk for BBB bonds, the AA spread, i.e. default risk for AA bonds, would also raise. On the other hand, no response to the BBB/AA disequilibrium can be noted for cat bonds, consistent with the fact that cat bonds are not sensitive to business cycle risk.

Given the aim of this study, error correction modeling has then focused on multiples only. In addition to lagged values (in changes) for cat bond multiples ($MULT$), the federal funds rate (FFR), and the spreads for AA and BBB corporate bonds (AA, BBB), we have also considered lagged changes for the 10-year US Treasury bond rate ($TB10Y$), the 3-month US Treasury Bills rate ($TB3M$) and the BB spread (BB), in order to investigate portfolio diversification effects related to changes in investors' preferences. Moreover, in order to assess investors' perception of evolving climate change risk, we have also considered past values for radiative forcing (RF), temperature volatility (h_{GL}), accumulated cyclones energy (ACE) and the Atlantic hurricanes Loss/Risk ratio

[17] The p-value for the Vector AR 1-2 test is 0.084; the p-value for the Vector Heteroskedasticity test is 0.200; the p-value for the Vector Normality test is 0.107.

[18] The analysis was repeated including also the BB spread and the US Treasury bills (TB3M) and bonds (TB10Y) rates. The empirical results confirm the separation of the cointegration space into three homogenous bivariate relationships involving FFR, TB10Y, TB3M and MULT, and into two bivariate relationships involving AA, BBB and BB. Details are available upon request from the authors.

(damages in 2017 constant US$ to ACE ratio; LR).[19]

In Table 3, Panel B, we report some alternative specifications for the error correction model, allowing to evaluate the incremental explanatory power of conditioning information relative to the inclusion of the error correction term alone. Hence, our econometric analysis of cat bond risk premium dynamics is based on the error correction model

$$\phi(L)\Delta MULT_t = c + \theta_0 \left[MULT_{t-1} - FFR_{t-1}\right] + \theta(L)\Delta z_t + \varepsilon_t \tag{17}$$

where $\varepsilon_t \sim i.i.d.N(0, \sigma^2)$, $\phi(L)$ and $\theta(L)$ are polynomials in the lag operator with all the roots outside the unit circle, $[MULT_{t-1} - FFR_{t-1}]$ is the error correction term, and $\Delta z_t = \Delta AA_t$, ΔBB_t, ΔBBB_t, ΔFFR_t, $\Delta TB3M_t$, $\Delta TB10Y_t$, ΔLR_t, RF_t, ACE_t, $h_{GL,t}$.

Given the small sample available, the analysis has considered up to five lags for each of the conditioning variables z_t at the time and a general to specific procedure for model reduction. As shown in the Table, all the models appear to be well specified according to standard misspecification tests, but only the inclusion of financial information yields a sizable increment in explanatory power relative to the benchmark model, particularly lagged BBB and BB spreads. In this respect, multiples appear to react to their disequilibrium with the FFR in the very short-term (within 1 year), then to corporate bonds spreads at the 2/3-year horizon, and then to Treasury bills and bonds rate changes at longer horizons (5-year). The above pattern is then consistent with the view associating falling multiples to the expansionary monetary stance pursued by the Fed, as well as to changes in the investors' preferences and portfolio shifts. Moreover, concerning the contribution of climate change variables, the latter either is not statistically significant, as for ACE and RF, or is significantly negative, as for h_{GL} and LR. Hence, it appears that climate change-related risk has not accurately been incorporated in cat bonds risk premia so far. In this respect, an increase in temperature volatility or in Atlantic hurricanes Loss/Risk ratio would be even followed by falling, rather than raising multiples in the medium-term. This appears to be inconsistent with the cat bonds market correctly pricing climate change risk.

In order to consider the contribution of the various conditioning variables jointly, a final error correction model has been specified by including all the lagged variables which were found significant in the partial error correction analysis above, i.e.

$$\Delta MULT_t = c + \theta_0 \left[MULT_{t-1} - FFR_{t-1}\right] + \boldsymbol{\theta}'\Delta \mathbf{g}_t + \varepsilon_t$$

where $\Delta \mathbf{g}_t = [\ \Delta AA_{t-2} \quad \Delta BB_{t-3} \quad \Delta BBB_{t-3} \quad \Delta TB3M_{t-5} \quad \Delta TB10Y_{t-5} \quad \Delta FFR_{t-5} \quad h_{GL,t-2} \quad \Delta LR_{t-5}\ ]'$ and $\boldsymbol{\theta}$ is the corresponding vector of parameters, i.e. $\boldsymbol{\theta} = [\ \theta_{2,AA} \quad \theta_{3,BB} \quad \theta_{3,BBB} \quad \theta_{5,TB3M} \quad \theta_{5,TB10Y} \quad \theta_{5,FFR} \quad \theta_{2,h_{GL}} \quad \theta_{5,LR}\ ]'$.

Its final specification, obtained through a general to specific reduction strategy, is reported in Table 3, Panel C. As shown in the Table, the final econometric model is very parsimonious, well specified and accounts for about 65% of $MULT$ variability.

In order to asses whether the latter performance might be due to overfitting, the model has been reestimated leaving out the last five observations (2013-2017); out of sample forecasts have then been generated by keeping constant the estimated parameters, and assessed by means of the RMSFE statistic; as reported in the Table, the final econometric model shows much higher forecasting accuracy than the model including the error correction term only; it also performs better than many of the other candidate

[19] Additional ADF test results are avaialble upon request from the authors.

partial specifications. We regard the latter results as evidence of stability and reliability of the estimated dynamic relationship.

In terms of determinants of $MULT$ short-run dynamics, the implications of the joint error correction analysis are consistent with the results of the partial one. In fact, a contraction in FFR would lead to a contraction in $MULT$ due to disequilibrium correction (monetary policy stance effect); moreover, an increase in the $TB3M - FFR$ spread would lead to a contraction in their return and risk premia ceteris paribus, possibly due to higher cat bonds demand. Some complementarity, rather than substitutability between Treasury Bills and cat bonds is however revealed by the joint analysis. Finally, the negative linkage between $MULT$ and LR is also confirmed. Accordingly, climate change-related risk appears not to have been accurately priced in the cat bonds market so far.

6 Conclusions

Since their introduction in the mid-1990s, the market for cat bonds has developed rapidly, achieving over US$ 30 billions of outstanding capital in 2017. Owner composition of cat bonds has also been changing over time: while in the early 2000s cat bonds were largely owned by hedge funds and reinsurance companies, currently institutional investors, including pension funds and mutual funds, own about 30% of total assets. These changes have also been coupled by a steady decline in the return per unity of risk or *multiple*, from a value of 8 in the early 2000s to a record low of 2 since 2015. Whether the latter pattern is consistent with current trends in natural disasters risk is an open question. This is particularly in the light of the large share of outstanding risk capital in the cat bonds market which faces some exposure to Atlantic hurricanes, a risk that climate change, among other disruptions, is expected to enhance (IPCC, 2012).

Hence, cat bonds risk assessment appears to require the investigation of the global warming phenomenon and of its potential implications for natural disasters severity. By means of a novel econometric framework, allowing for accurate modelling of first and second conditional moments of temperature anomalies, we find supporting evidence for the global warming hypothesis and for the existence of feedback effects for the natural environment. In particular, we find that the warming trend in temperature anomalies since the 1980s is driven by radiative forcing. We also find support for the view that global warming might affect the pattern of natural oscillations and enhance their disruptive effects. In this respect, we find that radiative forcing also drives the trend in SOI and ACE, and detect a sizable increase in SOI volatility since the mid-2000s, concurrent with the steepening in the radiative forcing trend and raise in temperature anomalies volatility. Hence, more intense and unstable ENSO phenomena and more disruptive Atlantic hurricanes activity can be expected as a consequence of global warming.

In the light of the ongoing contributions of human activity to radiative forcing and global warming, i.e., carbon dioxide, methane and aerosols emissions, natural disasters risk appears to be on a raising trend. Similarly on a raising trend is then also cat bonds risk, at least with reference to that sizable portion of outstanding capital exposed to climate change-related risk. Yet, the latter does not appear to have been properly incorporated in cat bonds multiples so far. In fact, while we find that falling cat bonds risk premia should be related to the expansionary monetary stance pursued by the Fed, as well as to some portfolio effects, we also find evidence of significant undervaluation of

natural disasters risk.

As an implication, it appears that cat bonds might not be a suitable diversification instruments for risk-adverse investors, such as pension funds. Moreover, due to risk undervaluation, the overall sanity of the market, as well as whether, in a not too far future, the cat bonds market might become a trigger for a new phase of generalized financial instability, appear to be important issues for investigation, which we leave for future research.

7 Appendix A1. Estimation of the SP-DCC model

Consistent and asymptotically Normal estimation is obtained by QML, following a multi-step procedure similar to Engle (2002). Hence, consider the Gaussian log-likelihood for the model in (1)-(2)

$$L = -\frac{1}{2}\sum_{t=1}^{T}\left(N\log(2\pi) + \log|\mathbf{H}_t| + \boldsymbol{\varepsilon}_t'\mathbf{H}_t^{-1}\boldsymbol{\varepsilon}_t\right), \tag{18}$$

which, following Engle (2002), is written as

$$\begin{aligned} L &= -\frac{1}{2}\sum_{t=1}^{T} N\log(2\pi) + 2\log|\mathbf{D}_t| + \boldsymbol{\varepsilon}_t'\mathbf{D}_t^{-1}\mathbf{D}_t^{-1}\boldsymbol{\varepsilon}) \\ &\quad -\frac{1}{2}\sum_{t=1}^{T}(-\mathbf{z}_t'\mathbf{z}_t + \log|\mathbf{R}_t| + \mathbf{z}_t'\mathbf{R}_t^{-1}\mathbf{z}_t) \end{aligned} \tag{19}$$

where

$$\mathbf{D}_t = diag\left(h_{1,t}^{1/2}, ..., h_{N,t}^{1/2}\right)$$

and the conditional correlation matrix $\mathbf{R}_t$ is defined as

$$\mathbf{R}_t = \mathbf{D}_t^{-1}\mathbf{H}_t\mathbf{D}_t^{-1}.$$

The log-likelihood function in (19) can then be decomposed into the sum of a *volatility part*

$$L_v(\boldsymbol{\theta}) = -\frac{1}{2}\sum_{t=1}^{T}\left(N\log(2\pi) + 2\log|\mathbf{D}_t| + \boldsymbol{\varepsilon}_t'\mathbf{D}_t^{-1}\mathbf{D}_t^{-1}\boldsymbol{\varepsilon}_t\right) \tag{20}$$

and a *correlation part*

$$L_C(\boldsymbol{\theta}, \boldsymbol{\phi}) = -\frac{1}{2}\sum_{t=1}^{T}\left(-\mathbf{z}_t'\mathbf{z}_t + \log|\mathbf{R}_t| + \mathbf{z}_t'\mathbf{R}_t^{-1}\mathbf{z}_t\right), \tag{21}$$

and estimation is performed in the following steps. Firstly, the mean equation model in (1) is estimated equation by equation by QML, i.e. the misspecified likelihood

$$L_m(\boldsymbol{\vartheta}) = -\frac{1}{2}\sum_{t=1}^{T}\sum_{i=1}^{N}\log(2\pi) + \log\sigma_i^2 + \frac{\varepsilon_{i,t}^2}{\sigma_i^2} \tag{22}$$

is maximized by separately maximizing each term.

Then, using the estimated conditional mean residuals $\hat{\boldsymbol{\varepsilon}}_t$, the volatility part of the likelihood (20) is maximized with respect to the conditional variance parameters; since (20) is the sum of individual GARCH likelihoods, i.e.

$$L_v(\boldsymbol{\theta}) = -\frac{1}{2}\sum_{t=1}^{T}\sum_{i=1}^{N}\log(2\pi) + \log h_{i,t} + \frac{\hat{\varepsilon}_{i,t}^2}{h_{i,t}}, \tag{23}$$

the volatility part is maximized by separately maximizing each term.

Finally, rather than maximizing the correlation part in (21), conditional to the estimated mean residuals and conditional variances delivered by the former two steps, $SP-DCC$ maximizes the sum of individual GARCH likelihoods for the aggregate series $y^{+}_{ij,t}$ and $y^{-}_{ij,t}$, i.e.

$$\begin{aligned} L_{SP}(\boldsymbol{\phi}) &= -\sum_{t=1}^{T}\sum_{i=1}^{N}\sum_{j>i}^{N}\left(\log(2\pi)+\log h^{+}_{ij,t}+\frac{\hat{\varepsilon}^{+2}_{ij,t}}{h^{+}_{ij,t}}\right) \\ &\quad -\sum_{t=1}^{T}\sum_{i=1}^{N}\sum_{j>i}^{N}\left(\log(2\pi)+\log h^{-}_{ij,t}+\frac{\hat{\varepsilon}^{-2}_{ij,t}}{h^{-}_{ij,t}}\right) \end{aligned} \tag{24}$$

which is jointly maximized by separately maximizing each term. Hence, the conditional variances for the aggregates $h^{+}_{ij,t}$, $h^{-}_{ij,t}$, $i,j=1,...,N$, $i\neq j$, are estimated equation by equation by means of QML, using the aggregates of the conditional mean residuals $\hat{\varepsilon}^{+}_{ij,t}=\hat{\varepsilon}_{i,t}+\hat{\varepsilon}_{j,t}$ and $\hat{\varepsilon}^{-}_{ij,t}=\hat{\varepsilon}_{i,t}-\hat{\varepsilon}_{j,t}$. The conditional covariances are then estimated by means of the polarization identity, i.e. the off-diagonal elements of $\mathbf{H}_t$, $h_{ij,t}$, $i,j=1,...,N$, $i\neq j$, are computed as

$$\hat{h}_{ij,t}=\frac{1}{4}\left[\hat{h}^{+}_{ij,t}-\hat{h}^{-}_{ij,t}\right] \qquad i,j=1,...,N \qquad i\neq j. \tag{25}$$

The conditional correlation matrix $\mathbf{R}_t$ is finally estimated as

$$\hat{\mathbf{R}}_t=\hat{\mathbf{D}}_t^{-1}\hat{\mathbf{H}}_t\hat{\mathbf{D}}_t^{-1} \tag{26}$$

where

$$\hat{\mathbf{D}}_t=diag\left(\hat{h}^{1/2}_{1,t},...,\hat{h}^{1/2}_{N,t}\right) \tag{27}$$

and the correlation part in (21) can be evaluated provided $\hat{\mathbf{R}}_t$ is positive definite at each point in time (see Morana (2015, 2017) for ex-post corrections that can be implemented in the case of a non positive definite correlation matrix).

Hence, the proposed approach to maximize the log-likelihood function is to find

$$\hat{\boldsymbol{\vartheta}}=\arg\max\left\{L_m\left(\boldsymbol{\vartheta}\right)\right\} \tag{28}$$

$$\hat{\boldsymbol{\theta}}=\arg\max\left\{L_v\left(\boldsymbol{\theta}\right)\right\} \tag{29}$$

$$\hat{\boldsymbol{\phi}}=\arg\max\left\{L_{SP}\left(\boldsymbol{\phi}\right)\right\} \tag{30}$$

and then use these values to evaluate $L_C(\boldsymbol{\theta},\boldsymbol{\phi})$.

It can be conjectured that, under standard regularity conditions, the asymptotic distribution of the QML estimator is

$$T^{1/2}\left(\hat{\boldsymbol{\psi}}-\boldsymbol{\psi}_0\right)\rightarrow N\{\mathbf{0},\mathbf{A}(\boldsymbol{\psi}_0)^{-1}\mathbf{B}(\boldsymbol{\psi}_0)\mathbf{A}(\boldsymbol{\psi}_0)^{-1}\} \tag{31}$$

where $\boldsymbol{\psi}_0=\left(\boldsymbol{\vartheta}_0',\boldsymbol{\theta}_0',\boldsymbol{\phi}_0'\right)'$ denotes the true value of the vector of parameters, $\mathbf{A}(\boldsymbol{\psi}_0)$ is the Hessian and $\mathbf{B}(\boldsymbol{\psi}_0)$ is the outer product gradient evaluated at the true parameter values. In fact, while the procedure does not maximize the joint log-likelihood in (19), consistent and asymptotically Normal estimation is however granted by the QML principle, under the standard assumptions. See Engle (2002) for additional details concerning the asymptotic distribution of the multi-step estimator; see also Morana (2017) for additional details on the asymptotic properties of the $SP-DCC$ estimator. As shown by the Monte Carlo exercise reported below, SP-DCC yields a similar or even superior performance to both ML and DCC in various parametric cases which are relevant for real data applications. Hence, $SP-DCC$ model represents a simple and valid candidate regardless of the fact that it is an approximate model in general.

8 Appendix A2: Small sample performance of SP-DCC

This section explores the performance of semiparametric DCC model (*SP-DCC*) of Morana (2015), together with other standard estimation methods. Hence, consider the following bivariate GARCH(1,1) model

$$\left[\begin{array}{c} y_{1t} \\ y_{2t} \end{array}\right] = H_t^{\frac{1}{2}} \left[\begin{array}{c} z_{1t} \\ z_{2t} \end{array}\right] \qquad \left[\begin{array}{c} z_{1t} \\ z_{2t} \end{array}\right] \sim i.i.dN(0, I_2) \tag{32}$$

where

$$H_t = \left[\begin{array}{cc} h_{1t} & h_{12t} \\ h_{12t} & h_{2t} \end{array}\right] \tag{33}$$

The conditional covariance matrix follows the following bivariate system

$$\begin{array}{rcl} \left[\begin{array}{cc} h_{1t} & h_{12t} \\ h_{12t} & h_{2t} \end{array}\right] & = & \left[\begin{array}{cc} \omega_1 & \omega_2 \\ \omega_2 & \omega_3 \end{array}\right] + \left[\begin{array}{cc} \beta_1 & \beta_2 \\ \beta_2 & \beta_3 \end{array}\right] \left[\begin{array}{cc} h_{1t-1} & h_{12t-1} \\ h_{12t-1} & h_{2t-1} \end{array}\right] \\ & & + \left[\begin{array}{cc} \alpha_1 & \alpha_2 \\ \alpha_2 & \alpha_3 \end{array}\right] \left[\begin{array}{cc} y_{1t-1}^2 & y_{1t-1}y_{2t-1} \\ y_{1t-1}y_{2t-1} & y_{2t-1}^2 \end{array}\right] \end{array} \tag{34}$$

That is, in its VECH form

$$\left[\begin{array}{c} h_{1t} \\ h_{12t} \\ h_{2t} \end{array}\right] = \left[\begin{array}{c} \psi_1 \\ \psi_2 \\ \psi_3 \end{array}\right] + \left[\begin{array}{ccc} \beta_1 & 0 & 0 \\ 0 & \beta_2 & 0 \\ 0 & 0 & \beta_3 \end{array}\right] \left[\begin{array}{c} h_{1t-1} \\ h_{12t-1} \\ h_{2t-1} \end{array}\right] + \left[\begin{array}{ccc} \alpha_1 & 0 & 0 \\ 0 & \alpha_2 & 0 \\ 0 & 0 & \alpha_3 \end{array}\right] \left[\begin{array}{c} y_{1t}^2 \\ y_{1t}y_{2t} \\ y_{2t}^2 \end{array}\right] \tag{35a}$$

As already shown by Bollerslev et al. (1988), it is possible to substitute $h_{it} = y_{it}^2 - \eta_{it}$ into (33) in order to obtain the VARMA representation for the squared processes

$$\begin{array}{c} \left[\begin{array}{ccc} (1-(\alpha_1+\beta_1)L) & 0 & 0 \\ 0 & (1-(\alpha_2+\beta_2)L) & 0 \\ 0 & 0 & (1-(\alpha_3+\beta_3)L) \end{array}\right] \left[\begin{array}{c} y_{1t}^2 \\ y_{1t}y_{2t} \\ y_{2t}^2 \end{array}\right] = \\ = \left[\begin{array}{c} \psi_1 \\ \psi_2 \\ \psi_3 \end{array}\right] + \left[\begin{array}{ccc} (1-\beta_1 L) & 0 & 0 \\ 0 & (1-\beta_2 L) & 0 \\ 0 & 0 & (1-\beta_3 L) \end{array}\right] \left[\begin{array}{c} \eta_{1t} \\ \eta_{2t} \\ \eta_{3t} \end{array}\right] \end{array} \tag{36}$$

where

$$E\eta_{it}^2 = E(z_{it}^2-1)^2 Eh_{it}^2 = \frac{(\kappa_i-1)h_i^2\left\{1-(\beta_i+\alpha_i)^2\right\}}{(1-\beta_i^2-2\alpha_i\beta_i-\alpha_i^2\kappa_i)}$$

and $\kappa_i = E\left(z_{i,t}^4\right)$.

The contemporaneous aggregation of model (36) leads to an ARMA(3,3) unless we observe that, for some i and j, $(\alpha_i+\beta_i) = (\alpha_j+\beta_j)$, i.e. unless we have the case of root cancellation. For example, consider the process $(y_{1t}+y_{2t})$ and assume $(\alpha_1+\beta_1) = (\alpha_2+\beta_2)$; then the contemporaneous aggregation of model (36) leads to an ARMA(2,2) for the squared aggregate $(y_{1t}+y_{2t})^2$, that is

$$\begin{array}{rl} & \left[1-\left(\left(\alpha_3+\beta_3\right)+\left(\alpha_1+\beta_1\right)\right)L+\left(\left(\alpha_3+\beta_3\right)\left(\alpha_1+\beta_1\right)\right)L^2\right]\left(y_{1t}^2+2y_{1t}y_{2t}+y_{2t}^2\right) \\ = & \psi+\left[\left(1-\left(\alpha_3+\beta_3\right)L\right)\left(1-\beta_1 L\right)\eta_{1,t}\right]+\left[\left(1-\left(\alpha_3+\beta_3\right)L\right)\left(1-\beta_2 L\right)2\eta_{2,t}\right] \\ & +\left[\left(1-\left(\alpha_1+\beta_1\right)L\right)\left(1-\beta_3 L\right)\eta_{3,t}\right], \end{array}$$

where $\psi = \left(1-\left(\alpha_3+\beta_3\right)\right)\left(\omega_1+2\omega_2\right)+\left(1-\left(\alpha_1+\beta_1\right)\right)\omega_3$.

In addition, when $(\alpha_1+\beta_1) = (\alpha_2+\beta_2) = (\alpha_3+\beta_3) = \gamma$, the aggregate process for the squared aggregate $(y_{1t}+y_{2t})^2$ is an ARMA(1,1)

$$
\begin{aligned}
& [1-\gamma L]\left(y_{1t}^2+2y_{1t}y_{2t}+y_{2t}^2\right) \\
= \quad & \phi+[1-\beta_1 L]\,\eta_{1,t}+[1-\beta_2 L]\,2\eta_{2,t}+[1-\beta_3 L]\,\eta_{3,t},
\end{aligned}
$$

where $\phi=\omega_1+2\omega_2+\omega_3$.

Similar findings hold for other combinations of (36), such as the squared difference process as considered by $SP-DCC$. Therefore, although the $SP-DCC$ model represents an approximation for this framework (DVECH-GARCH(1,1)), when the case of root cancellation arises this approximation gets more accurate. This seems to be the message from the following Monte Carlo simulation.

We generated model (32)-(33) using the following three parameters structures

$$
\begin{array}{l}
MODEL(i)\ for\ i=1,2,3 \\
\boldsymbol{\omega}_i=\left[\begin{array}{cc}\omega_1 & \omega_2\\ \omega_2 & \omega_3\end{array}\right]=\left[\begin{array}{cc}.01 & 0\\ 0 & .01\end{array}\right] \\
\boldsymbol{\alpha}_i=\left[\begin{array}{cc}\alpha_1 & \alpha_2\\ \alpha_2 & \alpha_3\end{array}\right]=\left[\begin{array}{cc}.1 & .1\\ .1 & .1\end{array}\right]+\left[\begin{array}{cc}U(0-x_i) & U(0-x_i)\\ U(0-x_i) & U(0-x_i)\end{array}\right] \\
\boldsymbol{\beta}_i=\left[\begin{array}{cc}\beta_1 & \beta_2\\ \beta_2 & \beta_3\end{array}\right]=\left[\begin{array}{cc}.9 & .9\\ .9 & .9\end{array}\right]-\boldsymbol{\alpha}+\left[\begin{array}{cc}U(0-x_i) & U(0-x_i)\\ U(0-x_i) & U(0-x_i)\end{array}\right] \\
with\ x_1=0.01\ \ x_2=0.03\ \ x_3=0.06
\end{array}
$$

We generated these models 2500 times. At each repetition, the matrices $\boldsymbol{\alpha}_i$ and $\boldsymbol{\beta}_i$ are randomly generated summing up a constant matrix and a random matrix whose elements have a random uniform distribution ranging from 0 through 0.01, 0.03 and 0.06 for MODEL(1), MODEL(2) and MODEL(3), respectively. This has been done in order to measure the impact of the departure from the possible root cancellation case on the small sample properties of $SP-DCC$. It is relevant to note that, when generating $\boldsymbol{\alpha}_i$ and $\boldsymbol{\beta}_i$, we allow only positive definite matrices since this condition guarantee that H_t is positive definite. We considered one sample size of 1000 observations. The simulation employed three alternative estimators: The multivariate (i.e. bivariate) GARCH ML estimator (ML), the ML-DCC (Engle, 2002; DCC) estimator and $SP-DCC$. In the Monte Carlo exercise we assess the ability of the various models to estimate the conditional correlation process $\rho_{12t}=h_{12t}/h_{1t}^{1/2}h_{2t}^{1/2}$, $t=1,...,1000$.

Results for the $RMSE$ of the conditional correlation, i.e. $RMSE=\left(\frac{1}{T}\sum_{t=1}^{1000}\left(\hat{\rho}_{12t}-\rho_{12t}\right)^2\right)^{1/2}$, are reported in the box-plots in Figure A1. Not surprisingly, ML has the best performance. DCC shows also a very good performance, comparable with ML; the performance of $SP-DCC$ is also comparable with the other methods, depending on the parameterization choice. This is notwithstanding $SP-DCC$ is an approximation for this specific framework. It is interesting to observe the change of performance across the different models. In particular, $SP-DCC$ tends to suffer when the gap between the $\alpha_i+\beta_i$ gets wider as in MODEL(3). On the other hand, for MODEL(1) the performance of $SP-DCC$ and DCC are very close, for MODEL(2) are similar, while some deterioration of $SP-DCC$ performance can be noted for MODEL(3). As the case of root cancellation is rather frequent in empirical applications, we expect MODEL(1) and MODEL(2) being indicative of the empirical performance of $SP-DCC$ with real data, where the sums $\alpha_i+\beta_i$ might even tend to approach one.

The Integrated GARCH process arises when $(\alpha_i+\beta_i)=1$. For this case, the $SP-DCC$ model is no more an approximation. Indeed, for this case, any combination of model (36) preserve the ARMA(1,1) parametrization and therefore any combination of y_{1t} and y_{2t} also preserve the IGARCH(1,1) structure. As a consequence $SP-DCC$ uses the correct specification to estimate the conditional correlations. These considerations have been tested through some Monte Carlo simulations.

We generated model (32)-(33) assuming that the conditional covariance matrix follows an Integrated GARCH dynamics (IGARCH(1,1)). We considered a single decay factor driving the dynamics of the conditional covariance such that the following three parameters structures are considered:

$$
\begin{array}{l}
MODEL(j)\ for\ j=4,5,6 \\
\boldsymbol{\omega}_j=0.0001*\left[\begin{array}{cc}1 & 1\\ 1 & 1\end{array}\right]+\left[\begin{array}{cc}U(0-x_j) & 0\\ 0 & U(0-x_j)\end{array}\right] \\
\boldsymbol{\alpha}_j=\left[\begin{array}{cc}0.05 & 0.05\\ 0.05 & 0.05\end{array}\right]+\left[\begin{array}{cc}U(0-x_j) & U(0-x_j)\\ U(0-x_j) & U(0-x_j)\end{array}\right],\ \boldsymbol{\beta}_j=\left[\begin{array}{cc}1 & 1\\ 1 & 1\end{array}\right]-\boldsymbol{\alpha}_j \\
with\ x_4=0.01\ \ x_5=0.03\ \ x_6=0.06
\end{array}
$$

The exercise compares the performance of four different competitors: 1) the pseudo-ML estimator as discussed in Zaffaroni (2008) that estimates a single decay factor (MLC), 2) the ML estimator that does not impose a single decay factor (ML), 3) $SP-DCC$ and 4) DCC. The reason for the inclusion of ML is that both $SP-DCC$ and DCC do not impose the single decay factor; we can then compare the performance of three estimators that do not know the data generation process. The empirical results are also reported in Figure A1. Since the performance of the models is unaffected by the selected parameterization, for reason of space we omit to report the results for the intermediate case (0.03). Beside MLC showing the best results, $SP-DCC$ always performs better than DCC and even ML. This confirms that when the IGARCH(1,1) framework arises, $SP-DCC$ represents a fully valid candidate in estimating the conditional correlations.

Now consider model (32)-(33) with the following unrestricted VECH representation:

$$\begin{bmatrix} h_{1t} \\ h_{12t} \\ h_{2t} \end{bmatrix} = \begin{bmatrix} \omega_1 \\ \omega_2 \\ \omega_3 \end{bmatrix} + \begin{bmatrix} \beta_1 & \beta_2 & \beta_3 \\ \beta_4 & \beta_5 & \beta_6 \\ \beta_7 & \beta_8 & \beta_9 \end{bmatrix} \begin{bmatrix} h_{1t-1} \\ h_{12t-1} \\ h_{2t-1} \end{bmatrix} + \begin{bmatrix} \alpha_1 & \alpha_2 & \alpha_3 \\ \alpha_4 & \alpha_5 & \alpha_6 \\ \alpha_7 & \alpha_8 & \alpha_9 \end{bmatrix} \begin{bmatrix} y_{1t}^2 \\ y_{1t}y_{2t} \\ y_{2t}^2 \end{bmatrix} \tag{37}$$

In this case neither the marginal processes y_{1t}^2, y_{2t}^2, $y_{1t}y_{2t}$, nor a combinations of them follows an ARMA(1,1) process. In addition, also the GARCH specifications of y_{1t} and y_{2t} do not follow a GARCH(1,1) model. For comparison purposes we generate the bivariate process as shown in Hafner (2008) p.476, in order to assess the performance of different competitors as above. Results comparing the $RMSE$ of the conditional correlations are shown in Figure A1. Note that the model in (37) has 21 parameters and this represents a challenge for ML estimation. Indeed, given the problem of convergence faced by the numerical optimization, due to the high number of parameters, we employ the true values of $\boldsymbol{\alpha}$ and $\boldsymbol{\beta}$ as initial values for the likelihood. This explains why the boxplot for the MLC is far below the others. Also in this exercise ML is the bivariate maximum likelihood estimator of a Diagonal VECH (as used before). In this framework ML is then an approximate ML or a QML estimator, as it estimates only the diagonal elements of model (37). Interestingly, $SP-DCC$ seems to slightly outperform both ML and DCC in this latter case. This is a very interesting and promising result, given that this framework represents the most unrestricted case.

Overall the Monte Carlo results are very promising: $SP-DCC$ model represents a simple and valid candidate regardless of the fact that it is an approximate model in general. Relative to competing approaches, such as the Engle (2002) DCC model, $SP-DCC$ has the advantage that can be implemented regardless of the cross-sectional sample size, i.e. also for the case of vast set of conditionally heteroskedastic time series.

References

[1] Angell, J.K., 1981. Comparison of variations in atmospheric quantities with sea surface temperature variations in the equatorial eastern Pacific. Monthly Wheather Review 109, 230-243.

[2] Bai, J., Perron, P., 1998. Estimating and testing linear models with multiple structural changes. Econometrica 66, 47-78.

[3] Bollerslev, T., 1990. Modeling the coherence in short-run nominal exchange rates: A multivariate generalized ARCH model. Review of Economics and Statistics 72, 498-505.

[4] Cai, W., Borlace S., Langaigne, M., van Rensch, P., Collins, M., Vecchi, G., Timmermann, A., Santoso, A., McPhaden, M.J., Wu., L., England, M.H., Wang, G., Guilyardi, E., Jin, F.-F., 2014. Increased frequency of extreme El Niño events due to greenhouse warming. Nature Climate Change 4, 1-6.

[5] Cai, W., Santoso A., Wang, G., Yeh, S.-W., An, S.-I., Cobb, K., Collins, M., Guuilyardi, E., Jin, F.-F., Kung, J.-S., Lengaigne, M., McPhaden, M.J., Takahashi, K., Timmermann, A., Vecchi, G., Watanabe, M., Wu., L., 2015a. ENSO and greenhouse warming. Nature Climate Change 5, 849-859.

[6] Cai, W., Wang, G., Santoso, A., McPhaden, M., Wu, L., Jin, F.-F., Timmermann, A., Collins, M., Vecchi., G., Langaigne, M., England, M.H., Dommenget, D., Takahashi, K., Guilyardi, E., 2015b.

Increased frequency of extreme La Nina events under greenhouse warming. Nature Climate Change 5, 132-137.

[7] Christy, J.R., McNider, R.T., 1994. Satellite greenhouse signal. Nature 367, 325.

[8] Cohen, J., Barlow, M., 2005. The NAO, AO and global warming: How closely related. Journal of Climate 18, 4498-4513.

[9] Coumou, D., Rahmstorf, S., 2012. A decade of weather extremes. Nature Climate Change 2, 1-6.

[10] Davies, P.J., 2017. Hurricane Irma Tests Risk-Reward of Catastrophe-Bond Market. The Wall Street Journal, 8 September 2017. Available at https://www.wsj.com/articles/hurricane-irma-tests-risk-reward-of-catastrophe-bond-market-1504895037.

[11] Douglass, D.H., Christy, J.R., 2009. Limits on CO_2 climate forcing from recent temperature data on earth. Energy and Environment 20, 177-189.

[12] Engle, R.F., 2002. Dynamic Conditional Correlation - A simple class of multivariate GARCH models. Journal of Business and Economic Statistics, 20, 339-350.

[13] Estrada, F., Perron, P., 2016. Extracting and analyzing the warming trend in global and hemispheric temperatures. Boston University, mimeo.

[14] Foster, G., Annan, J.D., Jones, P.D., Mann, M.E., Mullan, B., Renwick, J., Salinger, J., Schmidt, G.A., Trenberth, K.E., 2010. Comment on "Influence of the Southern Oscillation on tropospheric temperature". Journal of Geophysical Research 115, 1-4.

[15] Gallant, A.R., 1981. On the bias in flexible functional forms and an essentially unbiased form: the Fourier flexible form. Journal of Econometrics 15, 211-245.

[16] Gay, C., Estrada, F., Sánchez, A., 2009. Global and hemispheric temperatures revisited. Climatic Change 94, 333-349.

[17] Hafner, C.M., 2008. Temporal aggregation of multivariate GARCH models. Journal of Econometrics 142, 467-483.

[18] Hansen, J., Sato, M., Ruedy, R., Nazarenko, L., Lacis, A., Schmidt, G.A., Russell, G., Aleinov, I., Bauer, M., Bauer, S., Bell, N., Cairns, B., Canuto, V., Chandler, M., Cheng, Y., Del Genio, A., Faluvegi, G., Fleming, E., Friend, A., Hall, T., Jackman, C., Kelley, M., Kiang, N., Koch, D., Lean, J., Lerner, J., Lo, K., Menon, S., Miller, R., Minnis, P., Novakov, T., Oinas, V., Perlwitz, Ja, Perlwitz, Ju, Rind, D., Romanou, A., Shindell, D., Stone, P., Sun, S., Tausnev, N., Thresher, D., Wielicki, B., Wong, T., Yao, M., Zhang, S., 2005. Efficacy of climate forcing. Journal of Geophysical Research 110, 1-45.

[19] IPCC, 2012. *Managing the Risks of Extreme Events and Disasters to Advance Climate Change Adaptation. A Special Report of Working Groups I and II of the Intergovernmental Panel on Climate Change (IPCC).* Field CB, Barros V, Stocker TF, Qin D, Dokken DJ, Ebi KL, Mastrandrea MD, Mach KJ, Plattner G-K, Allen SK, Tignor M, Midgley PM (eds). Cambridge University Press, Cambridge, UK/New York.

[20] Jones, P.D., 1989. The influence of ENSO on global temperature. Climate Monitoring 17, 80-89.

[21] Kaufmann R.K., Kauppi, H., Mann, M.L., Stock, J.H., 2013. Does temperature contains a stochastic trend: linking statistical results to physical mechanisms. Climatic Change 118, 729-743.

[22] Kim, S.T., Cai, W., Jin, F.-F., Santoso, A., Wu, L., Guilyardi, E., An, S.I., 2014. Response of El Niño sea surface temperatures to greenhouse warming. Nature Climate Change 4, 786-790.

[23] Kosaka, Y., Xie, S.P., 2013. Recent global-warming hiatus tied to equatorial Pacific surface cooling. Nature 501, 403-407.

[24] McKitrick, R.R., Vogelsang, T.J., 2014. HAC robust trend comparisons among climate series with possible level shifts. Environmetrics 25, 528-547.

[25] Mills T.C., 2013. Breaks and unit roots in global and hemispheric temperatures: Aan updated analysis. Climatic Change 118, 745-755.

[26] Morana, C., 2015. Semiparametric estimation of multivariate GARCH models, Open Journal of Statistics 5, 852-858.

[27] Morana, C., 2017. Semiparametric estimation of vast conditional correlation matrices. University of Milan-Bicocca, mimeo.

[28] Ng, B., Cai, W. Walsh, K., Santoso, A., 2015. Nonlinear processes reinforce extreme IOD events. Scientific Reports 5, 1-10.

[29] Pretis, F., Mann, M.L., Kauffman, R.K., 2015. Testing competing models of the temperature hiatus: assessing the effects of conditioning variables and temporal uncertainties through sample-wide break detection. Climatic Change 131, 705-718.

[30] Schmith, T., Johansen, S., Thejll, P., 2012. Statistical analysis of global surface temperature and sea level using cointegration methods. Journal of Climate 25, 7822-7833.

[31] United Nations Office for the Coordination of Humanitarian Affairs, 2016. El Niño CERF-funded response in 2015-2016, 1 April 2016.

[32] Wigley, T.M.L., 2000. ENSO, volcanoes, amd record breaking temperatures, Geophysical Research Letters 27. 4101-4104.

[33] Zaffaroni, P., 2008. Large scale volatility models: Theoretical properties of professionals' practice. Journal of Time Series Analysis 29, 581-599.

Table 1: Adaptive-X-AR-GARCH models

Panel A: MX - Adaptive-X-AR model; Radiative forcing specification plus Bai-Perron break process									
	GL	**NH**	**SH**	**Trpcs**	**NoExt**	**SoExt**	**NoPol**	**SoPol**	**SOI**
c_0	-0.088 (0.041)	-0.111 (0.039)	-0.092 (0.020)	-0.083 (0.073)	-0.674 (0.191)	-0.495 (0.152)	-1.299 (0.361)	-	-
c_1	0.264 (0.055)	0.329 (0.055)	0.216 (0.039)	0.206 (0.096)	0.263 (0.064)	0.088 (0.048)	0.281 (0.113)	-	-
c_2	-	-	-	-	0.411 (0.144)	0.323 (0.113)	0.812 (0.275)	-	-
γ_3	-	-	-	-	-	-	0.156 (0.050)	-	-
γ_5 **or** γ_4 **(*)**	0.078 (0.032)	0.096 (0.036)	-	0.139(*) (0.036)	0.141 (0.032)	0.069 (0.024)	0.165 (0.053)	-	-0.436(*) (0.188)
δ_5 **or** δ_3 **(*)**	-	-	0.094 (0.025)	0.132(*) (0.076)	-	-	-	-	-
ϕ_1	0.564 (0.047)	0.500 (0.050)	0.497 (0.045)	0.859 (0.025)	0.368 (0.050)	0.334 (0.044)	0.184 (0.056)	0.335 (0.047)	0.455 (0.055)
ϕ_2	0.240 (0.045)	0.222 (0.046)	0.174 (0.044)	-	0.160 (0.047)	0.106 (0.047)	-	-	0.204 (0.057)
ϕ_3	-	-	-	-	-	-	-	-	0.116 (0.053)
β	0.990 (0.010)	0.990 (0.012)	0.990 (0.012)	0.990 (0.014)	0.990 (0.012)	0.990 (0.011)	0.990 (0.014)	0.990 (0.021)	0.990 (0.022)
α	0.010 (-)	0.010 (-)	0.010 (-)	0.010 (-)	0.010 (-)	0.010 (-)	0.010 (-)	0.010 (-)	0.010 (-)
Specification statistics									
R2	0.752	0.682	0.600	0.796	0.595	0.359	0.273	0.110	0.498
AIC	-1.5000	-0.8889	-1.0787	-0.9869	-0.3558	-0.5907	1.5408	1.7911	2.1068
BIC	-1.4549	-0.8438	-1.0336	-0.9599	-0.3016	-0.5365	1.5949	1.8001	2.1429
$Q(20)$	0.9353	0.9135	0.6127	0.0275	0.8735	0.7869	0.3675	0.3565	0.3509
$Q(20)_2$	0.6489	0.2659	0.7329	0.5170	0.0707	0.8722	0.1407	0.5623	0.0008
BJ	0.0312	0.0000	0.9880	0.0321	0.0107	0.3185	0.0000	0.1198	0.0000
Joint Bias	0.8749	0.5416	0.9806	0.1417	0.3203	0.2965	0.3068	0.6440	0.1412

Panel B: MXR - Adaptive-X-AR model; Radiative forcing specification									
	GL	**NH**	**SH**	**Trpcs**	**NoExt**	**SoExt**	**NoPol**	**SoPol**	**SOI**
c_0	-0.897 (0.205)	-1.059 (0.201)	-0.594 (0.170)	-0.632 (0.391)	-1.431 (0.142)	-0.758 (0.109)	-1.956 (0.244)	-	-
c_2	0.632 (0.135)	0.747 (0.133)	0.416 (0.109)	0.437 (0.255)	0.996 (0.094)	0.526 (0.070)	1.356 (0.163)	-	-
γ_3	-	-	-	-	0.121 (0.029)	0.046 (0.022)	0.217 (0.045)	-	-
γ_5 **or** γ_4 **(*)**	0.084 (0.034)	0.104 (0.039)		0.131(*) (0.074)	0.166 (0.032)	0.078 (0.035)	0.176 (0.055)	-	-0.436(*) (0.188)
δ_5 **or** δ_3 **(*)**	-	-	0.064 (0.028)	0.143(*) (0.075)	-	-	-	-	-
ϕ_1	0.574 (0.047)	0.512 (0.049)	0.521 (0.046)	0.862 (0.024)	0.370 (0.050)	0.331 (0.044)	0.206 (0.056)	0.335 (0.047)	0.455 (0.055)
ϕ_2	0.234 (0.046)	0.229 (0.046)	0.191 (0.043)	-	0.157 (0.049)	0.104 (0.046)	-	-	0.204 (0.057)
ϕ_3	-	-	-	-	-		-	-	0.116 (0.053)
β	0.990 (0.022)	0.990 (0.010)	0.990 (0.012)	0.990 (0.013)	0.990 (0.016)	0.990 (0.011)	0.990 (0.014)	0.990 (0.017)	0.990 (0.022)
α	0.010 (-)	0.010 (-)	0.010 (-)	0.010 (-)	0.010 (-)	0.010 (-)	0.010 (-)	0.010 (-)	0.010 (-)
Specification statistics									
R2	0.751	0.680	0.593	0.796	0.596	0.355	0.263	0.110	0.508
AIC	-1.4967	-0.8843	-1.0596	-0.9742	-0.3958	-0.5935	1.5502	1.7911	2.1068
BIC	-1.4516	-0.8391	-1.0145	-0.9291	-0.3416	-0.5393	1.5953	1.8003	2.1429
$Q(20)$	0.9232	0.8964	0.6648	0.0265	0.8914	0.7290	0.2659	0.3565	0.3509
$Q(20)_2$	0.3807	0.0482	0.7132	0.5139	0.0292	0.8184	0.1987	0.5623	0.0008
BJ	0.0443	0.0000	0.9143	0.0110	0.0062	0.3246	0.0000	0.1198	0.0000
Joint Bias	0.8330	0.6376	0.9832	0.1217	0.6360	0.5083	0.0622	0.6440	0.1412

Panel A reports the selected Adaptive-X-AR-GARCH models with radiative forcing control variables plus Bai-Perron step dummy variable (MX). Panel B reports the selected Adaptive-X-AR-GARCH models with radiative forcing control variables (MXR). R2 is the coefficient of determination. *AIC* and *BIC* are the Akaike and Bayes-Schwarz information criteria. $Q(20)$ and $Q(20)_2$ are the Box-Ljung test for serial correlation up to the 20*th* order in the standardized and squared standardized residuals, respectively. BJ is the Bera-Jarque normality test, Joint Bias is the Engle-Ng joint test for asymmetry in variance. The series investigated are average land and ocean temperature anomalies for the entire globe (GL; 90S-90N) and seven zones, namely the Northern Hemisphere (NH; 0-90N), the Southern Hemisphere (SH; 90S-0), the Tropics (Trpcs; 20S-20N), the Northern Extratropic (NoExt; 20N-90N), the Southern Extratropic (SoExt; 90S-20S), the Northern Polar (NoPol; 60N-90N), the Southern Polar (SoPol; 90S-60S).

Table 2: Dynamic models for Accumulated Cyclone Energy: 1984-2017

Panel A: Estimated dynamic models										
AR			**A-X-AR**					**A-X**		
					Long-run solution					**Long-run solution**
			γ_2	0.718 (0.168)	γ	0.185 (0.105)		γ_2	0.643 (0.163)	γ	0.141 (0.132)
			γ_3	-0.495 (0.168)	δ	0.160 (0.108)		γ_3	-0.504 (0.171)	δ	0.139 (0.126)
			δ_2	-0.517 (0.158)	θ	0.338 (0.171)		δ_2	-0.518 (0.162)	θ	0.511 (0.175)
			δ_5	0.710 (0.152)	σ_{LR}	0.561		δ_5	0.657 (0.151)	σ_{LR}	0.694
			θ_2	0.409 (0.184)				θ_2	0.511 (0.175)		
ϕ_1	0.306 (0.196)		ϕ_2	-0.211 (0.142)							
σ	1.044		σ	0.680				σ	0.694		
R^2	0.07		R^2	0.71				R^2	0.59		
AIC	2.9069		**AIC**	2.2786	**Wald**	0.023		**AIC**	2.2423	**Wald**	0.017
BIC	2.9967		**BIC**	2.5748				**BIC**	2.4667		
Log-Lik	-47-417		**Log-Lik**	-20.204				**Log-Lik**	-33.119		
***Q*(5)**	0.757		***Q*(5)**	0.391				***Q*(5)**	0.897		
***ARCH*(1)**	0.676		***ARCH*(1)**	0.221				***ARCH*(1)**	0.183		
BJ	0.097		***BJ***	0.802				***BJ***	0.51		

Panel B: Out of sample forecast statistics				
	2007-2017	**Rec. 2007-2017**	**2007-2016**	**Rec. 2007-2016**
RMSFE naive	1.104	1.104	1.085	1.085
RMSFE AR	0.888	0.890	0.768	0.762
Rel. RMSFE	0.804	0.806	0.708	0.703
RMSFE A-X-AR	0.703	**0.550**	0.674	**0.535**
Rel. RMSFE	0.637	**0.499**	0.621	**0.493**
RMSFE A-X	**0.679**	0.694	**0.612**	0.606
Rel. RMSFE	**0.615**	0.628	**0.564**	0.559

Panel A in the Table reports the estimated AR, A-X-AR and A-X models for ACE in standardized units. SE are reported in round brackets. R^2 is the coefficient of determination; AIC and BIC are the Akaike and Schwarz-Bayes information criteria, respectively; Log-Lik is the value of the log-likelihood function. The misspecification tests reported are the Box-Ljung serial correlation test (*Q*), the Engle ARCH test (*ARCH*), the Bera-Jarque Normality test (*BJ*). The specification test reported is the Wald test for the joint significance of the regressors in the solved static long-run equation. Panel B reports the root mean square forecast error (RMSFE) for eleven one-year ahead out of sample forecasts, from 2007 through 2017, computed using parameters estimated over the interval 1984-2006 (2007-2017) or by means of recursive estimation of the models, starting from the fixed sample 1979-2006, through the final sample 1979-2016 (Rec. 2007-2017); we also report the same statistics for the case of ten one-year ahead out of sample forecasts, from 2007 through 2016, i.e. excluding the forecast for (the outlying) year 2017 observation. In addition to the actual RMSFE figures, we also report relative RMSFE figures, obtained by dividing actual RMSFE figures by the RMSFE of the *naïve* (random walk) forecasting model (Rel. RMSFE).

Table 3: Cointegration properties and error correction modelling of cat bonds multiples.

Panel A: Integration and cointegration properties of cat bonds multiples					
ADF tests	**MULT**	**AA**	**BBB**	**FFF**	
no constant	-1.0456	-1.0215	-0.7960	-1.7574	
constant	-1.3480	-2.3273	-2.6233	-1.7475	
trend	-2.5126	-2.1607	-2.3906	-3.9245	
I(1) cointegration analysis					
Eigenvalues	**Log-Lik for**	**Rank**	**Trace test**	**Trace test (T-nm)**	
	-97.8181	**0**	85.10 [0.000]	68.08 [0.000]	
0.9187	-72.7283	**1**	34.92 [0.011]	27.93 [0.082]	
0.6000	-63.5649	**2**	16.59 [0.032]	13.27 [0.105]	
0.4687	-57.2402	**3**	3.940 [0.047]	3.150 [0.076]	
0.1789	-55.2691	**4**			
Unidentified cointegrating vectors (scaled on diagonal)					
MULT	1.000	0.133	-2.660	5.665	
AA	27.801	1.000	3.139	2.826	
BBB	-31.042	-0.053	1.000	-3.699	
FFR	-3.405	-0.037	2.077	1.000	
Identified cointegrating vectors			**Loadings**		
MULT	1.000	0.000	**MULT**	-0.164 (0.078)	-0.182 (0.309)
AA	0.000	-0.887 (0.079)	**AA**	-0.126 (0.034)	0.715 (0.133)
BBB	0.000	1.000	**BBB**	-0.195 (0.072)	-0.077 (0.287)
FFR	-1.359 (0.199)	0.000	**FFR**	0.177 (0.110)	-0.802 (0.435)
LR test	0.0237				
Restricted identified cointegrating vectors			**Loadings**		
MULT	1.000	0.000	**MULT**	-0.275 (0.093)	0.000
AA	0.000	-1.000	**AA**	-0.186 (0.038)	0.878 (0.069)
BBB	0.000	1.000	**BBB**	-0.249 (0.080)	0.000
FFR	-1.000	0.000	**FFR**	0.000	0.000
LR test	0.1174				

Panel B: Error correction models												Panel C: Final model	
	own	**AA**	**BBB**	**BB**	**FFR**	**TB3M**	**TB10Y**	**ACE**	**hGL**	**RF**	**LR**		
c	0.187 (0.254)	0.171 (0.299)	0.299 (0.191)	0.270 (0.250)	0.400 (0.232)	0.371 (0.240)	0.416 (0.255)	0.246 (0.255)	-0.128 (0.253)	1.039 (1.020)	0.161 (0.227)	c	0.265 (0.195)
θ_0	-0.182 (0.088)	-0.165 (0.107)	-0.231 (0.067)	-0.274 (0.102)	-0.238 (0.079)	-0.229 (0.081)	-0.211 (0.081)	-0.163 (0.089)	-0.180 (0.076)	-0.176 (0.090)	-0.167 (0.079)	θ_0	-0.204 (0.068)
θ_1	-	-	-	-	-	-	-	-	-	-	-	$\theta_{5,LR}$	-0.373 (0.129)
θ_2	-	0.474 (0.088)	-	-	-	-	-	-	-0.742 (0.308)	-	-	$\theta_{5,TB3M}$	-1.324 (0.534)
θ_3	-	-	0.243 (0.071)	0.555 (0227)	-	-	-	-	-	-1.339 (1.551)	-	$\theta_{5,FFR}$	1.324 (0.534)
θ_4	-	-	-	-	-	-	-	-	-	-	-		
θ_5	-	-	-	-	0.239 (0.097)	0.228 (0.105)	0.536 (0.267)	-0.202 (0.172)	-	-	-0.316 (0.152)		
R^2	0.246	0.476	0.617	0.583	0.497	0.458	0.436	0.324	0.492	0.289	0.445	R^2	0.644
AIC	1.9373	1.7053	1.3941	1.4786	1.6649	1.7408	1.7804	1.9612	1.6762	2.4685	1.7640	**AIC**	1.4534
BIC	2.0317	1.8469	1.5357	1.6202	1.8065	1.8824	1.9220	2.1028	1.8178	2.7136	1.9056	**BIC**	1.6422
Q(3)	0.164	0.0483	0.409	0.280	0.638	0.499	0.227	0.229	0.022	0.096	0.323	***Q(3)***	0.634
ARCH(1)	0.600	0.648	0.045	0.076	0.165	0.148	0.826	0.700	0.551	0.891	0.671	***ARCH(1)***	0.847
BJ	0.672	0.414	0.213	0.171	0.929	0.935	0.819	0.943	0.620	0.936	0.388	***BJ***	0.570
RMSFE	0.414	0.145	0.468	0.504	0.408	0.228	0.230	0.497	0.529	0.830	0.368	**RMSFE**	0.326

Panel A reports the results of the ADF non-stationarity test and of the Johansen cointegration analysis. The ADF test is reported for three different specifications of the deterministic component, i.e. no constant, constant, constant and trend. The Johansen Trace test statistic is reported with (T-nm) and without degrees of freedom correction, with p-values in squared brackets. Panel A finally reports the unidentified, identified and restricted identified cointegrating vectors and corresponding loadings. Standard errors are reported in round brackets. LR test is the LR test for overidentifying restrictions. Panel B reports error correction models including up to five lags of candidate financial and climatological conditioning variables (z_t) one at the time. The financial conditioning variables are the first differences of the AA, BB and BBB corporate spreads (AA, BB, BBB), the federal funds rate (FFR), the three-month Treasury bills rate (TB3M), the ten-year Treasury bonds rate (TB10Y), and the (standardized) Atlantic hurricanes Loss to Risk ratio (LR; damages in 2017 US $ to ACE ratio); the climatological variables are the accumulated cyclone energy intensity (ACE), radiative forcing (RF), and the global temperature anomaly volatility (h_{GL}). Panel C reports the final econometric model, whose starting specification includes, in addition to the constant and the error correction term, the eight significant variables as reported in Panel B. In the Table we also report the coefficient of determination (R^2), the Akaike and Bayes-Schwarz information criteria (AIC, BIC), the Box-Ljung serial correlation test (*Q*), the Engle ARCH test (*ARCH*), the Bera-Jarque Normality test (*BJ*), and the RMSFE for 1-step ahead out of sample forecasts generated over the period 2013-2017, using parameters estimated over the period 1997-2012.

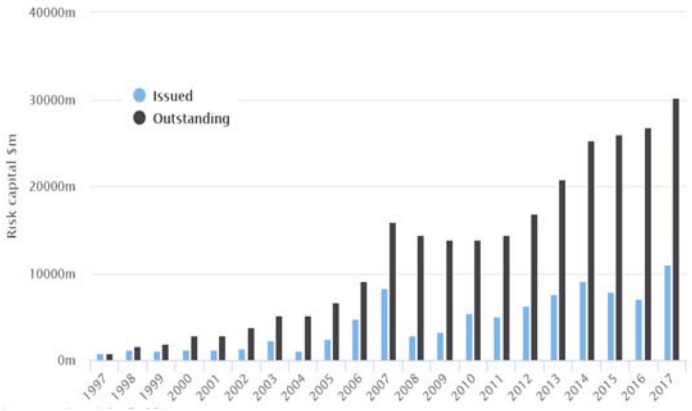

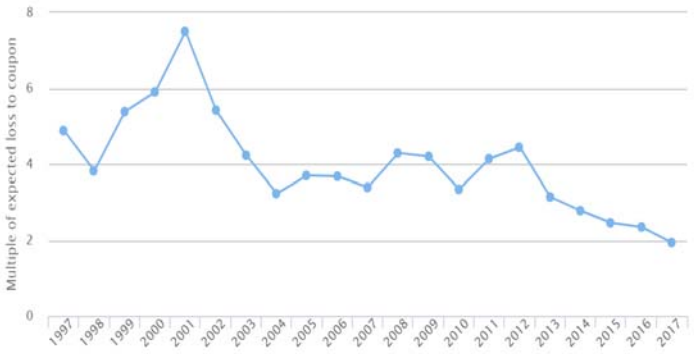

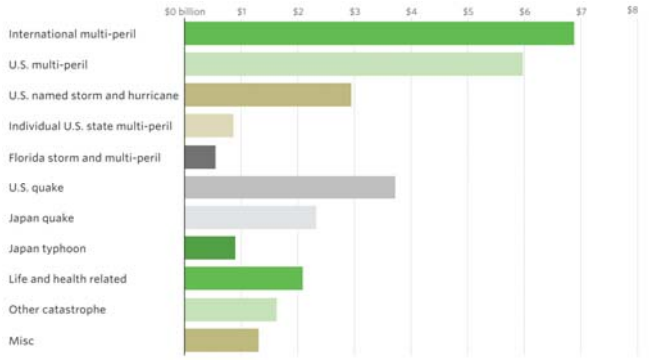

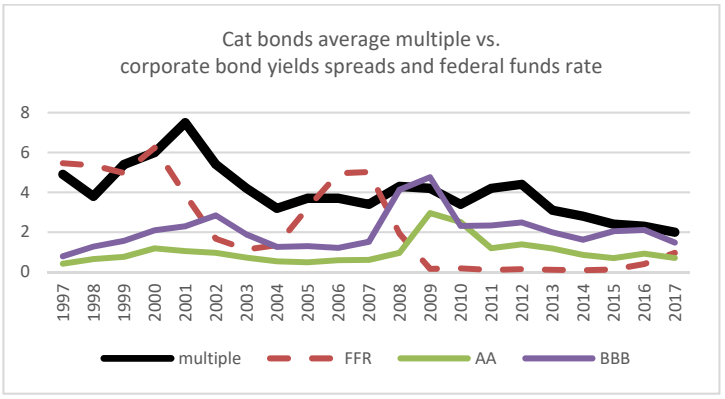

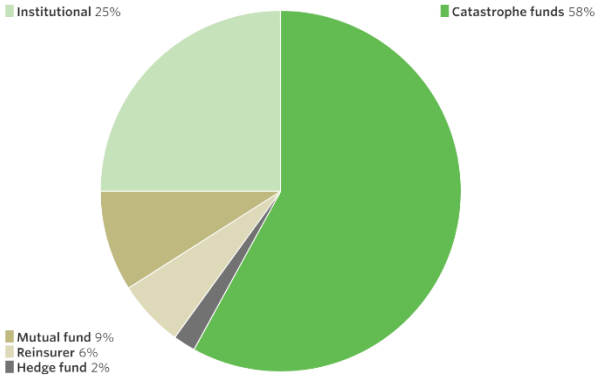

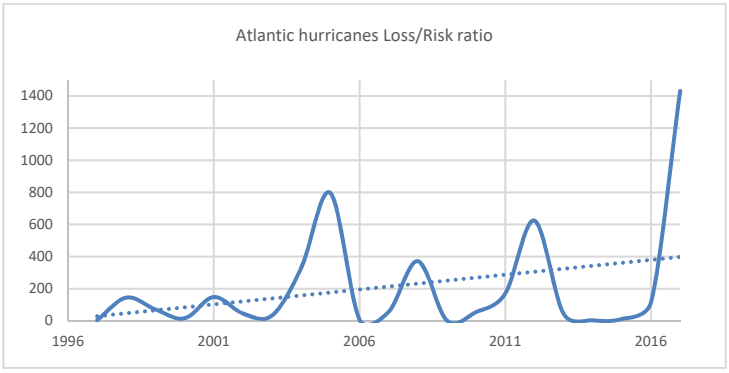

Figure 1: Catastrophe bonds and insurance-linked securities market. The top plot on the left-hand side reports figures for risk capital issued & outstanding per year. The center plot on the left-hand side reports figures for risk capital outstanding in year 2017 by type of exposure. The top plot on the right-hand side reports figures for the average multiple per year. The center plot on the right-hand side reports the cat bonds average multiple versus the effective federal funds rate (FFR) and various corporate spreads, i.e. the BofA Merrill Lynch US Corporate AA Option-Adjusted Spread (AA) and the BofA Merrill Lynch US Corporate BBB Option-Adjusted Spread (BBB). In all cases, the source for cat bonds figures is Artemis. The bottom plot on the left-hand side reports figures for investors in the cat-bonds market by ownership shares (Source: Aon Benfield Securities). The bottom plot on the right-hand side reports the Loss to Risk ratio for Atlantic hurricanes, as measured by the ratio of total damages (in 2017 constant US$) to accumulated cyclone energy (ACE in 10^4kt2).

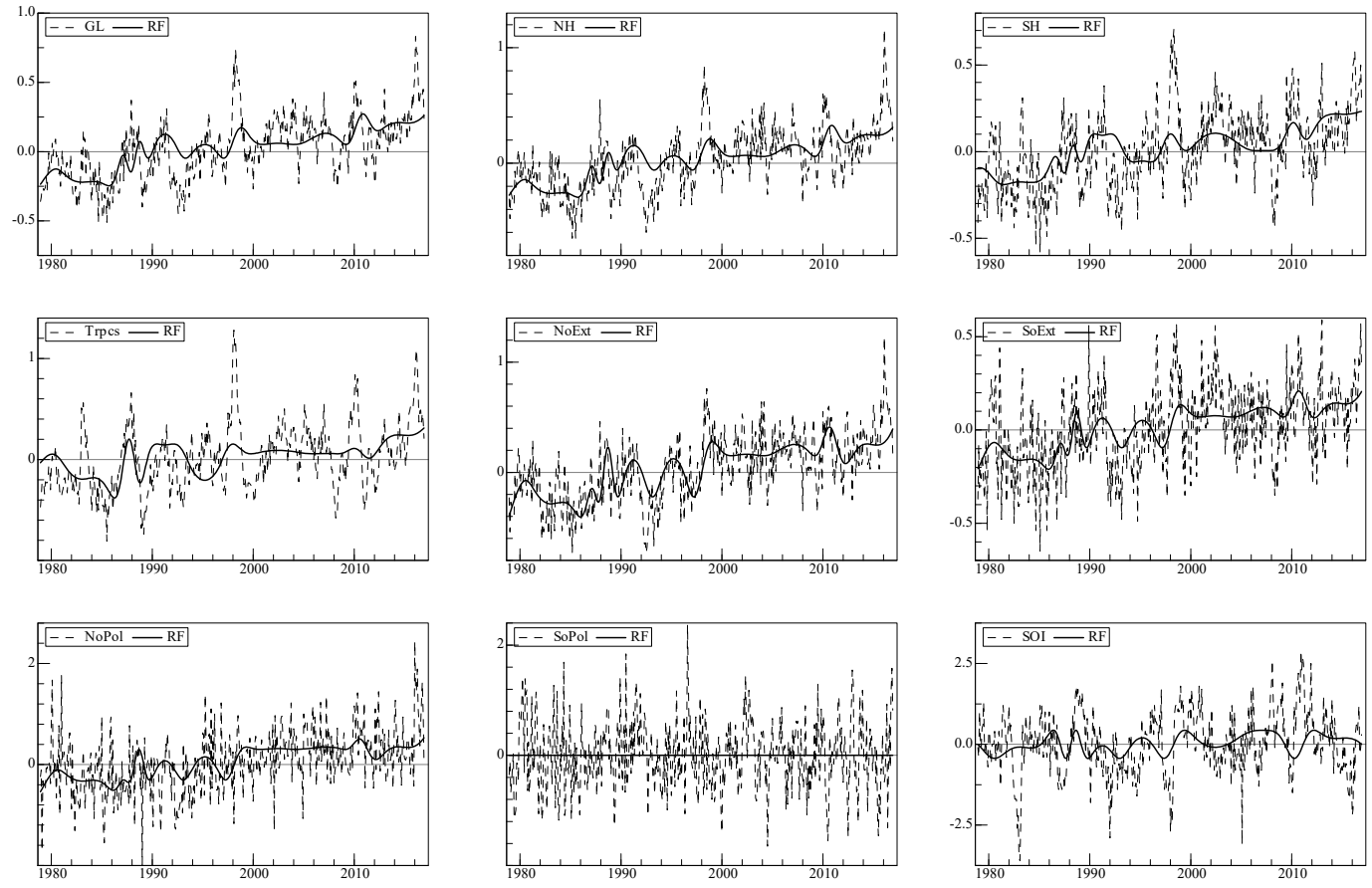

Figure 2: Temperature anomalies for the entire globe (GL; 90S-90N) and seven zones, namely the Northern Hemisphere (NH; 0-90N), the Southern Hemisphere (SH; 90S-0), the Tropics (Trpcs; 20S-20N), the Northern Extratropic (NoExt; 20N-90N), the Southern Extratropic (SoExt; 90S-20S), the Northern Polar (NoPol; 60N-90N), the Southern Polar (SoPol; 90S-60S). The Southern Oscillation Index is also plotted (SOI). For all series RF denotes the nonlinear trend associated with radiative forcing.

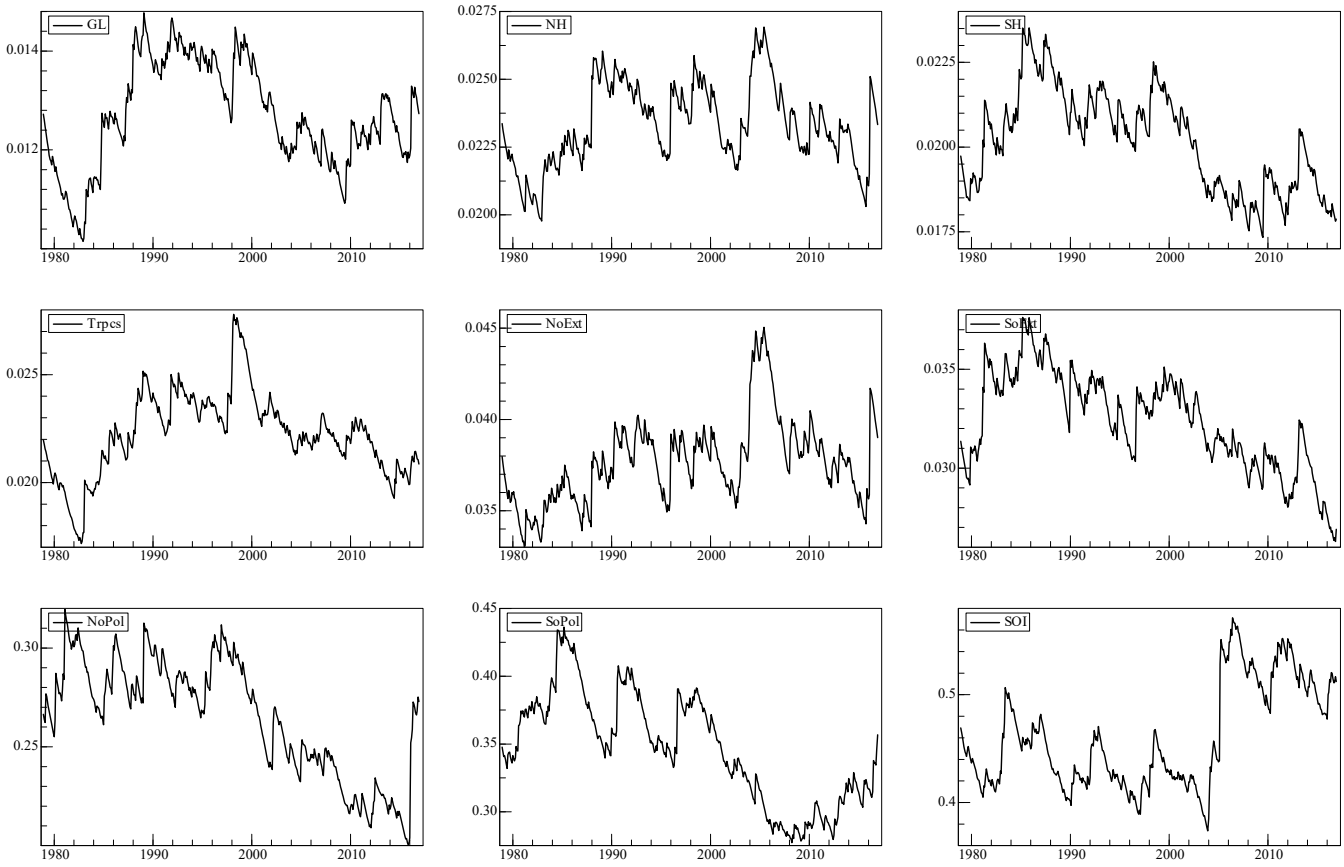

Figure 3: Estimated conditional variances of temperature anomalies for the entire globe (GL; 90S-90N) and seven zones, namely the Northern Hemisphere (NH; 0-90N), the Southern Hemisphere (SH; 90S-0), the Tropics (Trpcs; 20S-20N), the Northern Extratropic (NoExt; 20N-90N), the Southern Extratropic (SoExt; 90S-20S), the Northern Polar (NoPol; 60N-90N), the Southern Polar (SoPol; 90S-60S), the Southern Oscillation Index (SOI).

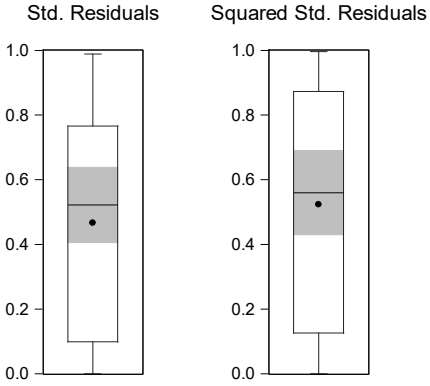

Figure 4: Boxplots for the p-values of the Box-Ljung tests carried out using standardized and squared standardized residuals.

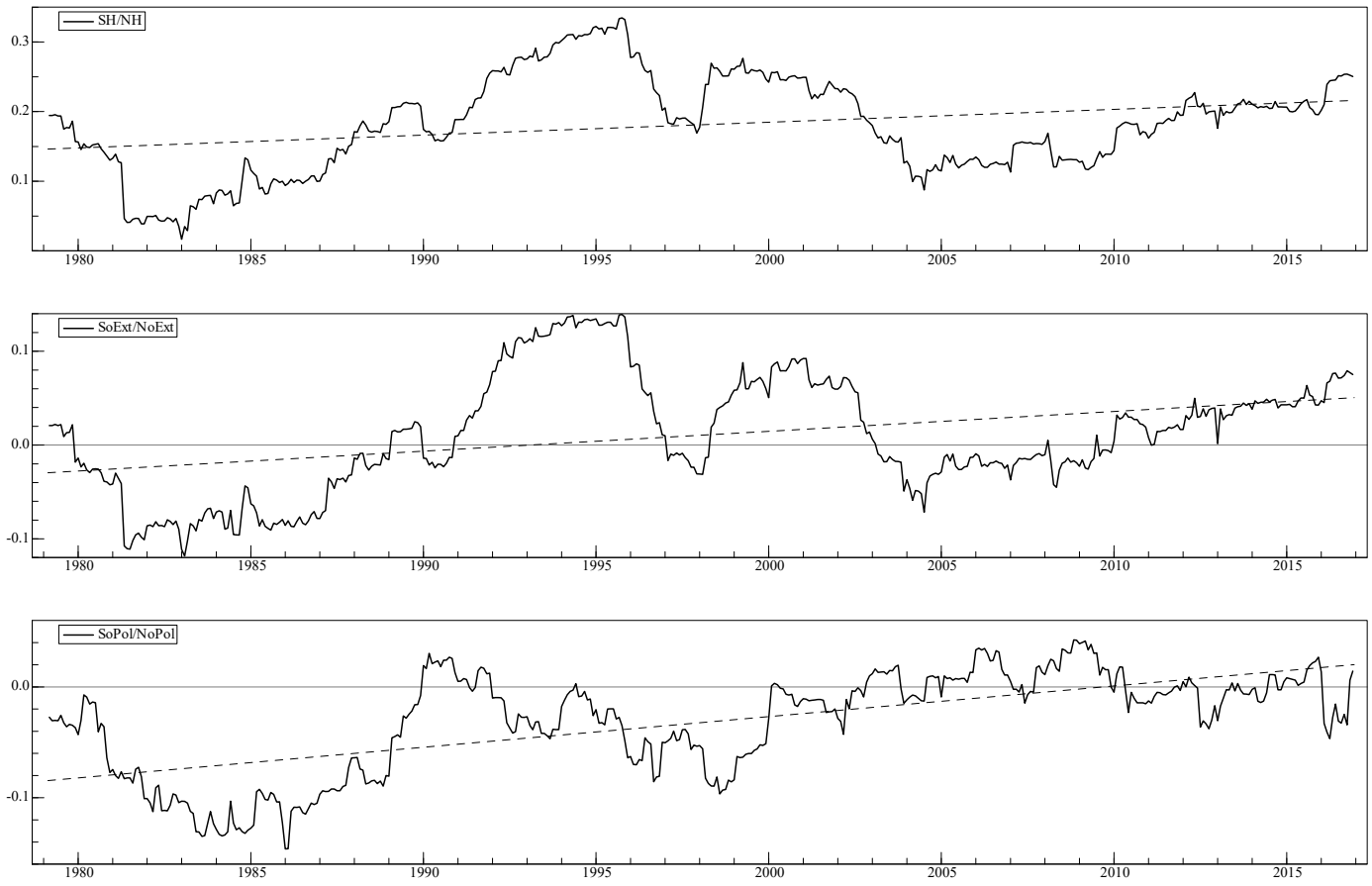

Figure 5: Conditional correlations of various temperature anomalies: the Northern Hemisphere versus the Southern Hemisphere (SH/NH), the Northern Extratropic versus the Southern Extratropic (SoExt/NoExt), the Northern Polar versus the Southern Polar (SoPol/NoPol).

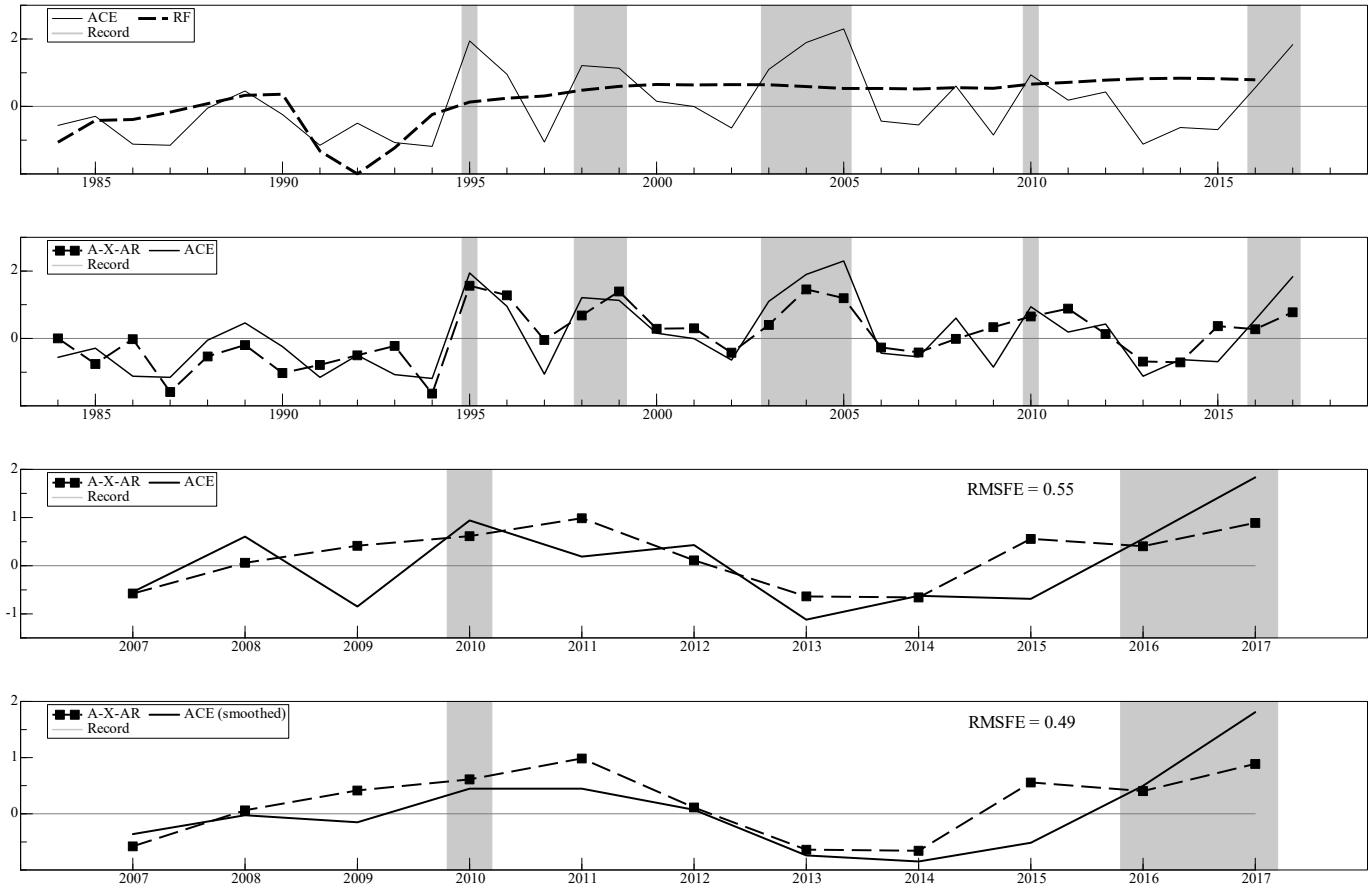

Figure 6: Accumulated cyclone energy (ACE) in standardized units: actual, fitted and forecasted values. The top plot reports actual values vs. radiative forcing (RF); the second plot report actual vs. Adaptive-X-AR (A-X-AR) fitted ACE values; the third plot shows actual vs. A-X-AR forecasted ACE values; the bottom plot shows (spline) smoothed ACE values vs. A-X-AR forecasted ACE values. The shaded areas denote selected record high ACE episodes.

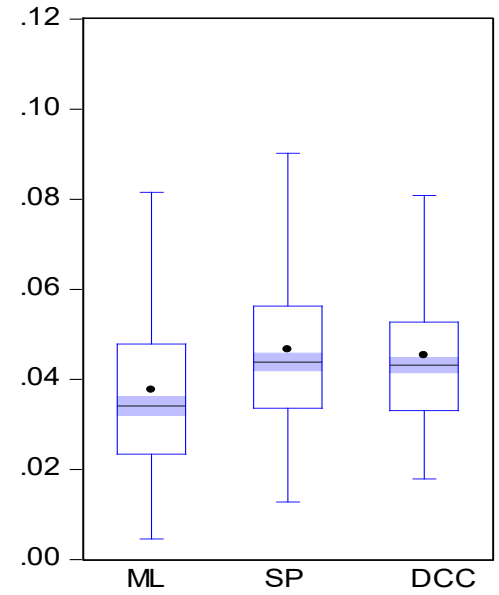

GARCH MODEL (1%)

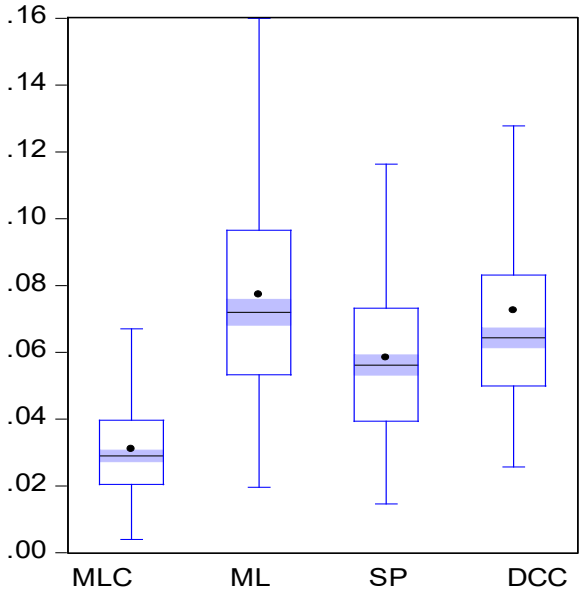

IGARCH MODEL (1%)

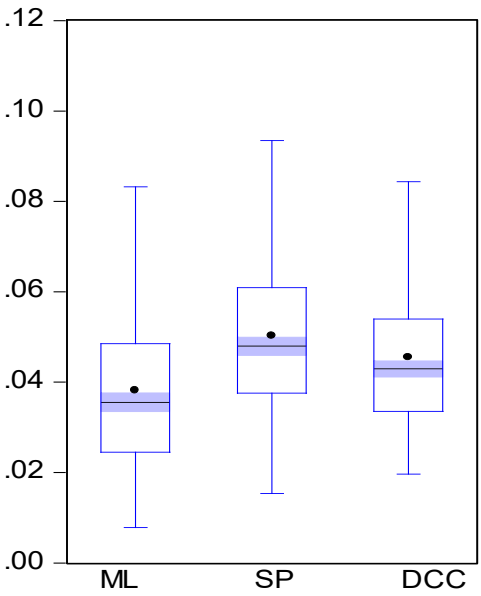

GARCH MODEL (3%)

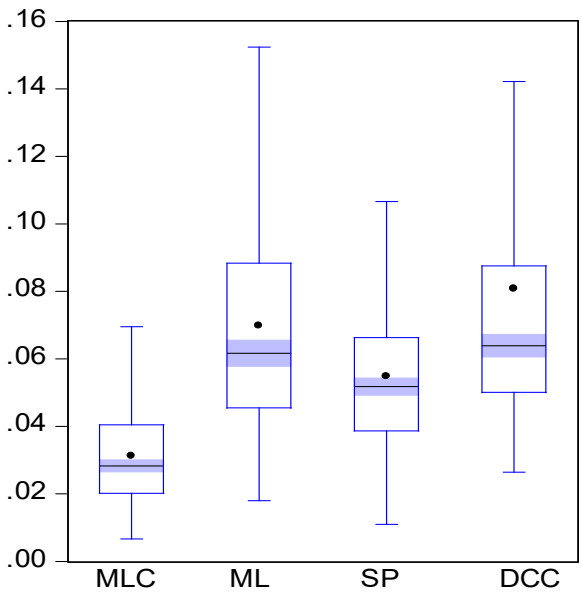

IGARCH MODEL (6%)

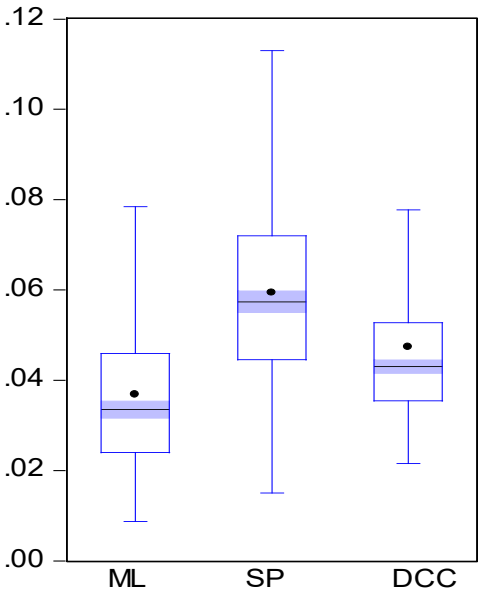

GARCH MODEL (6%)

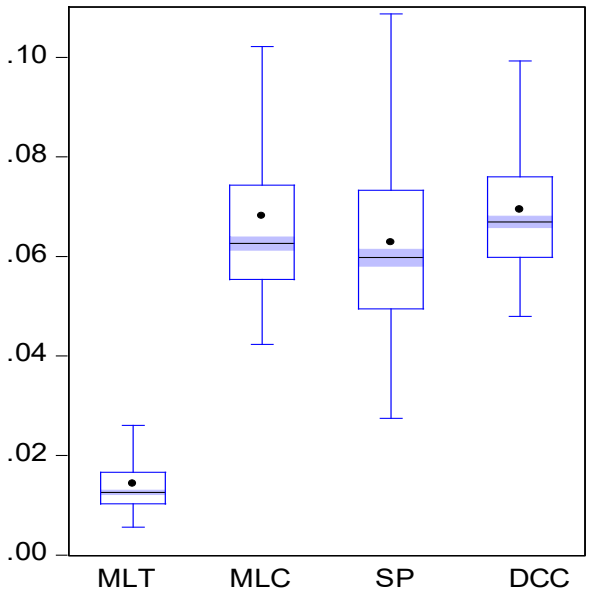

UVECH MODEL

Figure A1: Monte Carlo results. SP-DCC (SP) vs. Exact Maximum Likelihood (ML, MLT, MLC) and Engle DCC (DCC).

Supplementary Online Appendix to: "Some financial implications of global warming: An empirical assessment"

Claudio Morana[*,**], Giacomo Sbrana[+]

[*]Università di Milano Bicocca, CeRP-Collegio Carlo Alberto (Moncalieri, Italy)

and Rimini Centre for Economic Analysis (Rimini, Italy).

[+]NEOMA Business School

December 2017

Abstract

This Appendix presents additional details concerning forecasting and interpolation of radiative forcing data; the literature review on the econometric modelling of temperature anomalies and climate change; persistence properties of temperature anomalies and the modelling of the conditional mean function; the changing features of ENSO teleconnection.

[*]Address for correspondence: Claudio Morana, Università di Milano-Bicocca, Dipartimento di Economia, Metodi Quantitativi e Strategie di Impresa, Piazza dell'Ateneo Nuovo 1, 20126, Milano, Italy. E-mail: claudio.morana@unimib.it.

1 Forecasting and monthly interpolation of radiative forcing data

As radiative forcing data (RF) are available at the annual frequency and up to 2011 only, implementation of the Adaptive-ARMA-X models requires forecasting of radiative forcing data through 2016 and monthly interpolation. Concerning sample extension, forecasts over the period 2012 through 2016 have been generated by means of structural time series models specified for each of the various radiative forcing components; forecasts for total radiative forcing are then computed by aggregating the forecasts for the various components. Following Hansen et al. (2005), radiative forcing has been decomposed in various categories, i.e., Well-Mixed Greenhouse Gases ($WMGG$; carbon dioxide (CO_2), methane (NH4), nitrous oxide (N2O) and chlorofluorocarbons (CFCs)), Ozone ($O3$), Stratospheric Water Vapor ($StrH2O$), Reflective Tropospheric Aerosols ($ReflAer$), Tropospheric Aerosol Indirect Effects (AIE), Black Carbon Aerosols (BC), Snow Albedo ($snowAlb$), Stratospheric Aerosols ($StrAer$), Solar Irradiance ($Solar$), Land Use (including irrigation; $LandUse$). As we are interested in the modeling of the trend in radiative forcing, the Stratospheric Aerosols (StrAer) component is omitted from the forecasted aggregate. The latter series, over the sample of interest, is in fact heavily influenced by the major volcanic eruptions occurred in 1991 in the Philippines (Mt. Pitanubo) and in 1982 in Mexico (El Chichon), which lead to a sizable, temporary temperature "cooling" around the globe. Summary results for the estimated structural time series models and forecasted values for the radiative forcing components are reported in Table A1, Panel A. In all cases, apart from $Solar$, a local level linear trend model has been employed, i.e.

$$\begin{aligned} y_t &= \mu_t + \varepsilon_t & \varepsilon_t &\sim NID(0,\sigma_\varepsilon^2) \quad t = 1,2,...,T \\ \mu_t &= \mu_{t-1} + \beta_t + \eta_t & \eta_t &\sim NID(0,\sigma_\eta^2) \\ \beta_t &= \beta_{t-1} + \zeta_t & \zeta_t &\sim NID(0,\sigma_\zeta^2) \end{aligned}$$

where $y_t = WMGG$, $O3$, $StrH2O$, $ReflAer$, AIE, BC, $snowAlb$, $StrAer$, $LandUse$; ε_t, η_t and ζ_t are independent of one another. For $Solar$ the local linear trend model has been augmented by a stochastic cyclical component, i.e.

$$\begin{aligned} y_t &= \mu_t + \psi_t + \varepsilon_t \qquad t = 1,2,...,T \\ \begin{bmatrix} \psi_t \\ \psi_t^* \end{bmatrix} &= \rho \begin{bmatrix} \cos\lambda_c & \sin\lambda_c \\ -\sin\lambda_c & \cos\lambda_c \end{bmatrix} \begin{bmatrix} \psi_{t-1} \\ \psi_{t-1}^* \end{bmatrix} + \begin{bmatrix} \kappa_t \\ \kappa_t^* \end{bmatrix} \qquad \begin{matrix} \kappa_t \sim NID(0,\sigma_\kappa^2) \\ \kappa_t^* \sim NID(0,\sigma_\kappa^2) \end{matrix} \end{aligned}$$

where κ_t and κ_t^* are mutually independent. The above models can be estimated by ML and the Kalman Filter (see Harvey, 1989 for details). Forecasted values are reported in Figure A1.

Concerning monthly interpolation, we exploit the optimal approximation properties of the Fourier series. A monthly step function is then firstly constructed by holding constant the annual figures across the corresponding twelve months. Then, the step function series $y_{i,t}$ is regressed on the Gallant (1981) deterministic specification below by OLS

$$y_{i,t} = c_0 + c_1 t + \sum\nolimits_{i=1}^{p} \gamma_i \sin(2\pi i t/T) + \sum\nolimits_{i=1}^{p} \delta_i \cos(2\pi i t/T) \qquad (1)$$

where c_0 is an intercept term and $t = 1,...,T$ is a linear time trend. Estimation results are repored in Panel B.

The fitted process $\hat{y}_{i,t}$ yields the interpolated monthly radiative forcing series shown in Figure A2 (bottom plot, RHS), which has then been employed for the estimation of the Adaptive-ARMA-X models. As shown in the plot, forecasted values point to radiative forcing increasing through 2016, yet at slow pace; hence, the scenario might be considered conservative, potentially avoiding an upper bias in the estimated contribution of radiative forcing to global warming over the forecasted period. Moreover, the nonlinearly interpolated series track very closely the trend evolution of the annual radiative forcing series, supporting its use in the analysis. Additional support is provided by the robustness analysis reported in the paper.

2 The econometric modeling of anomalies and global warming: review of the literature

Persistence properties of temperature anomalies have been subject to careful assessment in the literature. There are two main competing views, differing in terms of the statistical model employed to account for the warming trend detected in the data, rather than for its attribution to causing factors. In fact, while it is in general agreed that the warming trend is determined by radiative forcing, both of natural and anthropogenic origin, its stochastic or deterministic nature is contended. On the one hand, Kaufmann et al. (2013) and Schmith et al. (2012) point to a stochastic trend in global and Northern (NH) and Southern (SH) hemisphere temperature anomalies, as generated by (and therefore cointegrating with) stochastic trends in radiative forcing components.[1] Feedback effects from temperature anomalies to radiative forcing have also been documented in this literature. For instance, Kaufmann et al. (2006) document a feedback loop in which temperature increases due to anthropogenic activities that emit greenhouse gases change flow to and from the atmosphere in a way that the radiative forcing of greenhouse gases is increased, generating a further increase in temperature. Schmith et al. (2012) also find that it is surface air temperature to adjust to the average temperature of the upper ocean, consistent with oceans' larger heating storage capacity. The latter finding is also consistent with the evidence of unidirectional Granger causality of temperature anomalies from SH to NH (Kaufmann and Stern, 1997; Harvey and Mills, 2001), due to the larger water content of SH relative to NH (and the different heating storage of water relative to land).

On the other hand, Estrada and Perron (2016) point to a common nonlinear deterministic trend in total radiative forcing and temperature anomalies, with significant breaks in slope in the 1960s and 1990s, and stationary fluctuations about trend. More precisely the first break is detected in 1962 (1968) and the second break in 1989 (1991) for NASA (HadCRUT4) data. This finding updates earlier evidence of trend stationarity and different timing in breaks for global and Northern and Southern hemispheres temperature anomalies, as reported by Gay et al. (2009) and Mills (2013)[2]. According to

[1] Earlier evidence on integration and cointegration properties of temperature anomalies can be found in Stern and Kaufmann (2000), Kaufmann and Stern (2002), Kaufmann et al. (2006), Mills (2006). See also Chang et al. (2016) for recent evidence from nonstationarity analysis extended to the density function of temperature anomalies.

[2] The break points detected by Gay et al. (2009) are 1977, 1985, 1911 for global, NH and SH temperature anomalies, respectively. The break points are also associated wit Earth orbit changes, solar irradiance and greenhouse gases concentrations. Mills (2013) updates the latter estimates to 1964 for SH temeperature and 1976 for both global and NH temperatures. See also Bloomfield (1992) and Zheng and Basher (1999) for earlier evidence of determininistic trends in temperature anomalies. See also Mills

Estrada and Perron (2016), the latter feature would be accounted by the contribution of natural variability oscillations such as the Atlantic Multidecadal Oscillation (AMO) for the Northern hemisphere and the Antarctic Oscillation (AAO or SAM) for the Southern hemisphere. Moreover, even the recent slowdown in the warming trend, i.e. the hiatus, might be related to radiative forcing, i.e. mostly to chlorofluorocarbons and methane reductions, rather than to natural variability factors such as AMO, PDO, ENSO, or lower solar activity, as claimed by Kosaka and Xie (2013). See also Pretis et al. (2015) on this issue. Estrada and Perron (2016) also update earlier evidence concerning persistence properties of temperature fluctuations about deterministic trends, which would be best described by a weakly stationary process. This contrasts with previous evidence of Bloomfield (1992) and Chung and Baillie (2002), pointing to stationary long memory fluctuations in global, NH and SH temperature anomalies about a linear deterministic trend. While long memory in temperature fluctuations might be an artifact due to a neglected slowly varying nonlinear trend function and/or alternating regimes/structural breaks as claimed by Mills (2006)[3], there also are valid reasons for this feature to be genuine, for instance, due to cross-sectional aggregation (Granger,1980) or to shocks of stochastic magnitude and duration (Parke, 1999). In the current framework, long memory could be determined by the cumulative effect of various radiative forcing mechanisms and/or the contribution of natural variability oscillations, such as ENSO, particularly in their most extreme manifestations.[4]

3 Testing for deterministic versus stochastic nonstationarity

In Table A2 we present the results of the persistence analysis for temperature anomalies. In the light of the available results in the literature, we test for stochastic nonstationarity versus trend stationarity/structural breaks. The analysis is carried out by means of the ADF test, also augmented with a nonlinear trend components (Enders and Lee, 2012); moreover, we implement the Perron et al. (2016) linearity Wald test and the Bai and Perron (1998) $UD-max$ and $SupF$ structural break tests.

As shown in Panel A, the null of stochastic nonstationarity is rejected by the ADF test for all the temperature anomalies and the SOI index at the usual significance levels, independently of the deterministic specification (no constant, constant, linear trend, nonlinear trend modelled by the Gallant (1981) trigonometric functional form). This finding is against earlier evidence of a unit root in temperature anomalies generated by I(1) trends in radiative forcing components, as for instance reported in Kaufmann et al. (2013) and Schmith et al. (2012); however, it is consistent with Estrada and Perron (2016), where a common nonlinear deterministic trend is found for temperature anomalies and radiative forcing. We have then implemented the Perron et al. (2016) Wald test for the presence of a nonlinear temporal trend (modelled by the Gallant (1981) functional form), which

(2006) for evidence of a more pronounced warming trend in NH temperatures since the 1970s, robust to stochastic or deterministic trend modeling.

[3]See Diebold and Inoue (2011) and references therein for a more general discussion on distinguishing deterministic nonstationarity and long memory. See also Rea et al. (2011) and Mann (2011) for recent views against the long memory feature.

[4]Pellettier and Turcotte (1997) also provides a theoretical explanation for the presence of long memory in temperature anomalies, based on an advection-diffusion model of the vertical transport of heat and water vapor in the atmosphere.

is valid under the assumption of both I(0) and I(1) disturbances. As shown in Panel B, the test rejects the null of no-nonlinearity for all the series, apart from Trpcs and SOI, when the linear deterministic trend is omitted from the Gallant (1981) functional form specification; on the other hand, less clear-cut evidence is found when the linear trend is included in the specification, suggesting that the two parts of the specification, i.e. the liner trend and the trigonometric component, might be substitute rather than complementary.

Since the Fourier specification closely approximates various forms of structural change (see Becker et al., 2006; Enders and Lee, 2012; Baillie and Morana, 2009, 2012; Perron et al., 2016), in order to further assess the nonlinearity issue, we have then directly tested for structural breaks using the Bai and Perron (1998) structural break tests. As shown in Panel C, consistent with McKitrick and Vogelsang (2014), Estrada and Perron (2016) and Gay et al. (2009), the $UD - max$ test points to a single break point. Similar to McKitrick and Vogelsang (2014), the break would be located about the mid-/end 1990s (1995 through 1998). The latter evidence is confirmed by the Bai and Perron (1998) $SupF$ test, which does not allow to reject the null hypothesis of a single break against the alternative of two breaks. Given its timing, the detected break point could be then related to the concurrent El Niño events (weak: 1995-1996; very strong: 1997-1998) and fading away of the cooling effect of the vulcanian eruption in the Philippines (Mt. Pinatubo in 1991).

Overall, the results of the persistence analysis are fairly clear-cut. In fact, the null of unit-root nonstationarity is rejected for all the anomalies (and SOI), in favor of a nonlinear deterministic (trend) component. Yet, whether the latter should be modelled by means of an abrupt level shift (single break dummy) or a smooth transition (trigonometric specification) requires further assessment, which is carried out below.

4 The specification of the conditional mean function

In the light of the results of the persistence analysis, we use a univariate Adaptive-ARMA (Baillie and Morana, 2012) specification for each of the N elements in the mean vector $\boldsymbol{\mu}_t(\boldsymbol{\delta})$,

$$\phi_i(L)\, y_{i,t} = c_{i,t} + \theta_i(L)\, \varepsilon_{i,t} \qquad i = 1, ..., N \tag{2}$$

where $\phi_i(L)$ and $\theta_i(L)$ are polynomials in the lag operator with all the roots outside the unit circle; $c_{i,t}$ is a level component specified according to various models nested in the general p-order Fourier function

$$c_t = c_0 + c_1 I_{bp} + c_2 t + \sum\nolimits_{i=1}^{p} \gamma_i \sin(2\pi i t/T) + \sum\nolimits_{i=1}^{p} \delta_i \cos(2\pi i t/T) \qquad \textbf{M0} \tag{3}$$

where c_0 is an intercept term; $I_{bp,t}$ is a step dummy variables with unitary values set according to the Bai and Perron (1998) structural break tests, as discussed above; $t = 1, ..., T$ is a linear time trend. The specification in (3) is very general and can approximate several functional forms; notice that the five below specifications are nested in (3), and obtained by imposing appropriate restrictions on the parameters:

$$c_t = \begin{cases} c_0 & c_1 = c_2 = \gamma_i = \delta_i = 0, i = 1, ..., p \quad \textbf{M1} \\ c_0 + c_1 I_{bp} & c_2 = \gamma_i = \delta_i = 0, i = 1, ..., p \quad \textbf{M2} \\ c_0 + c_2 t & c_1 = \gamma_i = \delta_i = 0, i = 1, ..., p \quad \textbf{M3} \\ c_0 + c_1 I_{bp} + c_2 t & \gamma_i = \delta_i = 0, i = 1, ..., p \quad \textbf{M4} \\ c_0 + c_1 t + \sum_{i=1}^{p} \gamma_i \sin(2\pi i t/T) + \sum_{i=1}^{p} \delta_i \cos(2\pi i t/T) & c_2 = 0 \quad \textbf{M5} \end{cases} \tag{4}$$

Hence, M1 is the constant level model, M2 is the constant level plus break dummy model, M3 is the constant level plus linear trend model, M4 nests model M2 and M3, and M5 is the Gallant flexible functional form (Gallant, 1981). The Adaptive-ARMA model has the advantage of allowing for flexible modeling of low frequency fluctuations and structural change, given the ability of the Gallant (1981) flexible functional form to approximate a very general class of nonlinear functions (see Becker et al., 2006; Enders and Lee, 2012; Baillie and Morana, 2009, 2012; Perron et al., 2016). The latter deterministic specification has also been recently employed by Estrada and Perron (2016) with the same purpose.

Rather than in the time trend variable t, the p-order Fourier approximation can be expressed in terms of a variable believed to determine the overall level of temperature anomalies; in our application the latter variable is represented by radiative forcing (RF), consistent with the available evidence of a common trend in temperature anomalies and radiative forcing (Kaufmann et al., 2013; Schmith et al., 2012; Estrada and Perron, 2016); hence, the general p-order Fourier approximation becomes

$$c_t = c_0 + c_1 I_{bp} + c_2 RF_t + \sum_{i=1}^{p} \gamma_i \sin(2\pi i RF_t^*) + \sum_{i=1}^{p} \delta_i \cos(2\pi i RF_t^*) \quad \textbf{MX} \tag{5}$$

where $RF_t^* = \frac{RF_t - \min RF_t}{\max RF_t - \min RF_t}$ is RF_t scaled to range between 0 and 1. Similarly to (3), various models are nested in (5); in addition to the M1 and M2 models above, in particular one has

$$c_t = c_0 + c_2 RF_t + \sum_{i=1}^{p} \gamma_i \sin(2\pi i RF_t^*) + \sum_{i=1}^{p} \delta_i \cos(2\pi i RF_t^*) \quad c_2 = 0 \quad \textbf{MXR}$$

The Adaptive-X-ARMA specification yield by (2)-(5) shows the same desirable properties of the Adaptive-ARMA model yield by (2)-(3) in terms of flexible modeling of low frequency fluctuations in temperature anomalies; it is however likely to better tracking the trend in temperature anomalies, in the case the latter is determined by radiative forcing.

4.1 Model selection results

The most general specifications of the mean model are the Adaptive-ARMA model in (2) with level term c_t as in (3), i.e. M0, and the Adaptive-X-ARMA model, where the level term c_t is as in (5), i.e. MX. Model selection is then carried out considering all the nested deterministic specifications, i.e. M1 through M5 and MXR.

In all cases a parsimonious AR(2) model is selected according to a general to specific model selection strategy, apart from Trpcs and SoPol (AR(1)) and SOI (AR(3)). Moreover, consistent with the results of the Perron et al. (2016) Wald test, only low order

Fourier terms in the time trend variable are statistically significant. In particular, a first order sine expansion appears to be appropriate for all temperature anomalies apart from SoPol, for which a third order cosine term is selected. Moreover, for SOI no trigonometric term is significant (not reported).[5] On the other hand, Fourier terms in the radiative forcing variable of order three to five are selected for all models, apart from SoPol (see Table 1 in the paper for details).

Since all the models are equivalent in terms of misspecification tests, model selection is then performed by means of information criteria.[6] As shown in Table A3, Panel A, the Adaptive-X-AR models (MX or MXR) are always preferred to their corresponding Adaptive-AR models (M0 or M5), apart from SoPol. The most general Adaptive-X-AR model MX is selected by both the AIC and BIC information criteria for GL, NH, SH, NoPol; it is also selected for Trpcs, yet by the AIC only. Moreover, the Adaptive-X-AR model neglecting the break dummy, i.e. MXR, is selected for NoExt and SoExt by both criteria, and for SOI by the AIC only. In only three cases the BIC selects the constant intercept model M1 as best model (Trpcs, SoPol, SOI).

The clear-cut selection of the Adaptive-X-AR models appears to be consistent with previous results in the literature, where structural breaks in temperature anomalies are related to either the contribution of natural oscillations such as the Atlantic Multidecadal Oscillation (AMO) for the Northern hemisphere and the Antarctic Oscillation (AAO or SAM) for the Southern hemisphere (Estrada and Perron, 2016), or to the effects of radiative forcing (natural or human made), such as changing solar irradiance and greenhouse gases concentrations (Gay et al., 2009).

Finally, while no evidence of misspecification is detected for the homoskedastic version of the Adaptive-AR and Adaptive-X-AR models (not reported), as shown in Table A3, Panel B, allowing for GARCH effects in the conditional variance always leads to a better model according to the BIC criterion. In this framework, the selection of the Adaptive-X-AR models is even more clear-cut than before, as the Adaptive-AR model (M1) is only selected for SoPol. The findings are consistent with the presence of a dynamic structure in second moments, which, possibly due to observational noise, remains undetected by standard misspecification tests.

5 ENSO teleconnection and changing anomalies pattern

In Figures A2-A3 we plot the estimated (contemporaneous) conditional correlations across temperature anomalies and SOI. For comparison we also include the Oceanic Niño Index (ONI). The latter is the standard that the National Oceanic and Atmospheric Administration - US Department of Commerce (NOAA) uses for identifying El Niño (warm) and La Niña (cool) events in the tropical Pacific.[7]

As shown in Figure A2, interesting patterns are revealed by the correlation analysis, yielding information on ENSO teleconnection and its evolving properties. Firstly, the conditional correlation of SOI versus the Tropics is mostly negative in sign, consistent

[5] A full set of results is available from the authors upon request.

[6] Details about misspecification tests are available from the authors upon request.

[7] The ONI is computed as the running 3-month mean SST anomaly for the Niño 3.4 region (i.e., 5^oN-5^oS, 120^o-170^oW). Data are available at http://www.cpc.noaa.gov/products/analysis_monitoring/ensostuff/ensoyears.shtml.

with the effects of El Niño (La Niña) events. In fact, a *contraction* (increase) in SOI, i.e. an El Niño (La Niña) event, is associated with an *increase* (reduction) in temperature at the Tropics above (below) normal levels. Interestingly, the very strong El Niño events of 1982 and 1997-1998 have made the conditional correlation more negative (up to -0.2), i.e. they have enhanced the heat transfer; this holds true also since the end of 2000s. The latter findings are consistent with the general recognition that ENSO is an asymmetric phenomenon and that extreme ENSO events are different from moderate events (Cai et al., 2015a,b; 2014; Kim et al., 2014). The asymmetric feature of ENSO can be also clearly detected globally and at the poles, i.e. for GL/SOI, SoPol/SOI and NoPol/SOI, coherent with the working of the "atmospheric bridge", which also have become more sizably negative during the episodes of interest.[8]

Moreover, as shown in Figure A3, a pattern consistent with ENSO teleconnection is also shown by the conditional correlations relating Trpcs with the other zones. Conditional correlations are in fact positive over the whole sample for Trpcs with NoExt and SoExt (0.10); less clear-cut are the correlations with the poles; for instance, while the correlation with NoPol is mostly positive, the opposite can be noted for SoPol, apart from the last part of the sample, i.e. since about 2010. Overall, the pattern appears to be consistent with a warming shock being transmitted from the Tropics to the other zones, i.e. to the Extratropics and then the Poles. Coherent with the asymmetric feature of ENSO, the transmission of heat shocks gets stronger with the magnitude of the shock. See, for instance, the sizable increase in the correlations observed during the 2014-2016 very strong El Niño event.

References

[1]

[2] Bai, J., Perron, P., 1998. Estimating and testing linear models with multiple structural changes. Econometrica 66, 47-78.

[3] Baillie, R.T., Chung, S-K., 2002. Modeling and forecasting from trend-stationary long memory models with application to climatology. International Journal of Forecastig 18, 215-226.

[4] Baillie, R.T., Morana, C., 2009. Modeling long memory and structural breaks in conditional variances: An Adaptive FIGARCH approach. Journal of Economic Dynamics and Control 33, 1577-1592.

[5] Baillie, R.T., Morana, C., 2002. Adaptive ARFIMA models with applications to inflation, Economic Modelling 29, 2451-2459.

[6] Becker, R., Enders, W., Lee, J., 2006. A stationarity test in the presence of an unknown number of smooth breaks. Journal of Time Series Analysis 27, 381-409.

[7] Bloomfield, P., 1992. Trends in global temperature. Climatic Change 21, 1-16.

[8] Chang, Y., Kaufmann, R.K., Kim, C.S., Miller, J.I., Park, J.Y., Park, S., 2016. Time series analysis of global temperature distributions: Identifying and estimating persistent features in temperature anomalies. Boston University, mimeo.

[9] Enders, W., Lee, J., 2012. A unit root test using a Fourier series to approximate smooth breaks. Oxford Bulletin of Economics and Statistics 74. 574-599.

[8] Heat shocks at the tropics are transmitted Northward and Southward through the generation of planetary or Rossby waves, that propagate poleward and are subsequently refracted back from the pole to the tropics.

[10] Engen,E.M., Laubach, T., Reifschneider, D., 2015. The macroeconomic effects of the Federal Reserve's unconventional monetary policies. Finance and Economics Discussion Series 2015-005. Washington: Board of Governors of the Federal Reserve System.

[11] Estrada, F., Perron, P., 2016. Extracting and analyzing the warming trend in global and hemispheric temperatures. Boston University, mimeo.

[12] Gallant, A.R., 1981. On the bias in flexible functional forms and an essentially unbiased form: the Fourier flexible form. Journal of Econometrics 15, 211-245.

[13] Gay, C., Estrada, F., Sánchez, A., 2009. Global and hemispheric temperatures revisited. Climatic Change 94, 333-349.

[14] Granger, C.W.J., 1980. Long memory relationships and the aggregation of dynamic models. Journal of Econometrics 14, 227-238.

[15] Hansen, J., Sato, M., Ruedy, R., Nazarenko, L., Lacis, A., Schmidt, G.A., Russell, G., Aleinov, I., Bauer, M., Bauer, S., Bell, N., Cairns, B., Canuto, V., Chandler, M., Cheng, Y., Del Genio, A., Faluvegi, G., Fleming, E., Friend, A., Hall, T., Jackman, C., Kelley, M., Kiang, N., Koch, D., Lean, J., Lerner, J., Lo, K., Menon, S., Miller, R., Minnis, P., Novakov, T., Oinas, V., Perlwitz, Ja, Perlwitz, Ju, Rind, D., Romanou, A., Shindell, D., Stone, P., Sun, S., Tausnev, N., Thresher, D., Wielicki, B., Wong, T., Yao, M., Zhang, S., 2005. Efficacy of climate forcing. Journal of Geophysical Research 110, 1-45.

[16] Harvey, D.I., Mills, T.C., 2001. Modeling global temperature using cointegration and smooth transitions. Statistical Modeling 1, 143-159.

[17] Harvey, A.C., 1989. *Forecasting, Structural Time Series and the Kalman Filter.* Cambridge University Press, Cambridge, UK/New York.

[18] Kaufmann, R.K., Stern, D.I., 1997. Evidence for human influence on climate from hemispheric temperature relations. Nature 388, 39-44.

[19] Kaufmann, R.K., Stern, D.I., 2002. Cointegration analysis of hemisphere temperature relations. Journal of Geophysical Research 107, 1-10.

[20] Kaufmann R.K., Kauppi, H., Stock, J.H., 2006. The relationship between radiative forcing and temperature: what do statistical analyses of instrumental temperature record measure? Climatic Change 77, 279-289.

[21] Kaufmann R.K., Kauppi, H., Mann, M.L., Stock, J.H., 2013. Does temperature contains a stochastic trend: linking statistical results to physical mechanisms. Climatic Change 118, 729-743.

[22] Kim, S.T., Cai, W., Jin, F.-F., Santoso, A., Wu, L., Guilyardi, E., An, S.I., 2014. Response of El Niño sea surface temperatures to greenhouse warming. Nature Climate Change 4, 786-790.

[23] Kosaka, Y., Xie, S.P., 2013. Recent global-warming hiatus tied to equatorial Pacific surface cooling. Nature 501, 403-407.

[24] McKitrick, R.R., Vogelsang, T.J., 2014. HAC robust trend comparisons among climate series with possible level shifts. Environmetrics 25, 528-547.

[25] Mills T.C., 2006. Modelling current trends in Northern Hemisphere temperatures. International Journal of Climatology 26, 867-884.

[26] Mills T.C., 2013. Breaks and unit roots in global and hemispheric temperatures: Aan updated analysis. Climatic Change 118, 745-755.

[27] Parke, W.R., 1999. What is fractional integration? The Review of Economics and Statistics 81,632-638.

[28] Perron, P., Shintani, M, Yabu, T., 2016. Testing for flexible nonlinear trends with an integrated or stationary noise component. Oxford Bulletin of Economics and Statistics, forthcoming.

[29] Pretis, F., Mann, M.L., Kauffman, R.K., 2015. Testing competing models of the temperature hiatus: assessing the effects of conditioning variables and temporal uncertainties through sample-wide break detection. Climatic Change 131, 705-718.

[30] Schmith, T., Johansen, S., Thejll, P., 2012. Statistical analysis of global surface temperature and sea level using cointegration methods. Journal of Climate 25, 7822-7833.

[31] Stern D.I., Kaufmann, R.K., 2000. Detecting a global warming signal in hemispheric series: A structural time series analysis. Climatic Change 47, 411-438.

[32] Zheng, X., Basher, R.E., 1999. Structural time series models and trend detection in global and regional temperature series. Journal of Climate 12, 2347-2358.

Table A1: Modelling, forecasting and interpolation of radiative forcing data

Panel A: Annual structural time series models for radiative forcing										
	WMGG	**O3**	**StrH2O**	**ReflAer**	**AIE**	**BC**	**snowAlb**	**StrAer**	**LandUse**	**Solar**
Stand. Dev.										
σ_η	0.0055 (0.0005)	0.0055 (0.0001)	0.0000 (-)	0.0002 (0.0000)	0.0005 (0.0001)	0.0002 (0.0001)	0.0005 (0.0001)	0.4529 (0.028)	0.0001 (0.0000)	0.0043 (0.0049)
σ_ς	0.0032 (0.0006)	0.0005 (0.0001)	0.0001 (0.0000)	0.0012 (0.0001)	0.0001 (0.0001)	0.0011 (0.0001)	0.0004 (0.0001)	0.0000 (-)	0.0002 (0.0001)	0.0006 (0.0003)
σ_ε	0.0000 (-)	0.0001 (0.0000)	0.0003 (0.0000)	0.0004 (0.0001)	0.0001 (0.0000)	0.0003 (0.0000)	0.0001 (0.0000)	0.0000 (-)	0.0003 (0.0001)	0.0084 (0.0014)
σ_ψ	-	-	-	-	-	-	-	-	-	0.0081 (0.0117)
ρ	-	-	-	-	-	-	-	-	-	0.981 (0.007)
R_d^2	0.839	0.822	0.375	0.951	0.877	0.865	0.704	0.015	0.345	0.584
Forecasts										
2012	3.065 (0.007)	0.216 (0.001)	0.063 (0.001)	-1.454 (0.002)	-1.025 (0.001)	0.601 (0.001)	0.204 (0.001)	-0.114 (0.455)	-0.093 (0.001)	0.213 (0.018)
2013	3.105 (0.013)	0.216 (0.001)	0.063 (0.001)	-1.472 (0.003)	-1.038 (0.003)	0.609 (0.003)	0.206 (0.001)	-0.115 (0.645)	-0.093 (0.001)	0.223 (0.025)
2014	3.144 (0.019)	0.216 (0.002)	0.063 (0.001)	-1.489 (0.005)	-1.050 (0.004)	0.616 (0.004)	0.209 (0.002)	-0.116 (0.793)	-0.093 (0.001)	0.212 (0.031)
2015	3.183 (0.025)	0.216 (0.003)	0.063 (0.001)	-1.507 (0.007)	-1.063 (0.006)	0.623 (0.006)	0.212 (0.003)	-0.117 (0.920)	-0.093 (0.001)	0.185 (0.034)
2016	3.223 (0.032)	0.216 (0.004)	0.063 (0.001)	-1.525 (0.010)	-1.076 (0.008)	0.630 (0.008)	0.214 (0.003)	-0.114 (1.032)	-0.093 (0.002)	0.150 (0.036)

Panel B: Gallant (1981) interpolating function					
c_0	1.100 (0.007)	γ_1	0.039 (0.005)	δ_1	-0.055 (0.002)
c_1	0.002 (0.000)	γ_2	-0.022 (0.003)	δ_2	-
		γ_3	-0.045 (0.003)	δ_3	0.040 (0.002)
		γ_4	0.035 (0.003)	δ_4	-0.017 (0.002)
		γ_5	-	δ_5	-0.023 (0.002)
R^2	0.994				

Panel A reports the estimated standard deviation of the level, slope, irregular and cyclical components, the estimated damping parameter for the cyclical components, the coefficient of determination computed for the first difference of the series, and the forecasts over the period 2012 through 2016. The series investigated are the various radiative forcing components in W/m2, i.e. Well-Mixed Greenhouse Gases (WMGG), Ozone (O3), Stratospheric Water Vapor (StrH2O), Reflective Tropospheric Aerosols (ReflAer), Tropospheric Aerosol Indirect Effects (AIE), Black Carbon Aerosols (BC), Snow Albedo (snowAlb), Stratospheric Aerosols (StrAer), Solar Irradiance (Solar), Land Use (including irrigation; LandUse). Panel B reports the estimated parameter, with HACSE standard errors in round brackets, for the Gallant (1981) interpolating function.

Table A2: Persistence analysis of temperature anomaly series

Panel A: ADF tests									
	GL	**NH**	**SH**	**Trpcs**	**NoExt**	**SoExt**	**NoPol**	**SoPol**	**SOI**
Fourier	-5.780	-6.750	-7.220	-5.680	-8.250	-10.00	-12.20	-15.00	-6.720
Constant+Trend	-5.737	-6.684	-7.200	-5.910	-8.141	-7.104	-9.243	-15.01	-5.877
Constant	-4.493	-4.607	-4.738	-5.174	-4.637	-5.876	-6.126	-15.03	-5.780
No costant	-4.418	-4.543	-4.684	-5.104	-4.583	-5.811	-6.024	-14.86	-5.699
Panel B: Nonlinearity Wald test									
Linear trend included	**GL**	**NH**	**SH**	**Trpcs**	**NoExt**	**SoExt**	**NoPol**	**SoPol**	**SOI**
Order 1	0.212	0.153	0.388	0.244	0.470	0.377	0.454	0.239	0.753
Order 2	1.833	2.355	1.660	0.602	2.535	1.694	**3.609**	0.232	0.446
Order 3	0.446	0.619	0.507	0.118	0.723	2.271	0.410	2.419	2.216
Order 4	1.790	3.114	1.009	0.700	**5.733**	1.914	0.902	1.285	2.266
Order 5	1.377	0.831	2.169	0.682	0.436	**3.245**	**3.359**	**4.033**	0.462
Linear trend omitted	**GL**	**NH**	**SH**	**Trpcs**	**NoExt**	**SoExt**	**NoPol**	**SoPol**	**SOI**
Order 1	**5.346**	**7.228**	**5.018**	1.704	**6.349**	**5.202**	**24.371**	0.188	1.618
Order 2	0.276	0.333	0.388	0.490	0.121	0.250	0.007	0.245	0.279
Order 3	0.714	0.697	1.223	0.319	0.412	2.553	0.020	2.647	2.604
Order 4	0.600	0.792	0.465	1.608	0.370	0.289	0.025	1.398	1.717
Order 5	0.282	0.077	0.475	0.313	0.029	0.501	0.087	**4.499**	0.305
Panel C: Structural break analysis									
	GL	**NH**	**SH**	**Trpcs**	**NoExt**	**SoExt**	**NoPol**	**SoPol**	**SOI**
UD-max	44.120	92.867	33.397	64.821	103.22	34.724	41.711	33.939	42.709
SupF(2|1)	9.087	7.124	9.793	7.677	8.724	11.431	10.227	3.023	12.855
Break dates	**1997:6**	**1997:8**	**1995:3**	**1997:6**	**1998:1**	**1997:6**	**1995:3**	**1995:3**	**1995:3**

Panel A reports the ADF non-stationarity tests for four different specifications of the deterministic component, i.e. constant, trend and first order Fourier expansion; constant and trend; constant; no constant and trend. The 5% and 1% critical values are -4.28 and -4.84, -3.42 and -3.98, -2.87 and -3.45, -1.94 and -2.57, respectively. Panel B reports the Perron-Shintani-Yabu nonlinearity Wald test for various orders of the Fourier expansion (from 1 to 5). The critical values are 3.219, 4.605, 5.992, 9.210 for the 20%, 10%, 5% and 1% critical value, respectively. Panel C reports the results of the Bai-Perron (1998) UD-Max structural break test. The 5% and 1% critical values of the test are 9.63 and 13.58, respectively. It also reports the SupF test for the null of 1 break against the alternative of 2 breaks; the 5% and 1% critical values of the test are 11.14 and 15.03, respectively. The date of the selected break point is reported in the last row of the table. The series investigated are average land and ocean temperature anomalies for the entire globe (GL; 90S-90N) and seven zones, namely the Northern Hemisphere (NH; 0-90N), the Southern Hemisphere (SH; 90S-0), the Tropics (Trpcs; 20S-20N), the Northern Extratropic (NoExt; 20N-90N), the Southern Extratropic (SoExt; 90S-20S), the Northern Polar (NoPol; 60N-90N), the Southern Polar (SoPol; 90S-60S).

Table A3: Adaptive-AR and Adaptive-X-AR models

Panel A: Conditionally homoskedastic models										
		GL	**NH**	**SH**	**Trpcs**	**NoExt**	**SoExt**	**NoPol**	**SoPol**	**SOl**
M0	**AIC**	-1.4943	-0.8864	-1.0570	-0.9681	-0.3652	-0.5681	1.5457	1.8013	2.1169
	BIC	-1.4312	-0.8232	-0.9938	-0.9140	-0.3020	-0.5049	1.6089	1.8555	2.1801
M1	**AIC**	-1.4748	-0.8569	-1.0325	-0.9714	-0.3068	-0.5270	1.6295	1.7901	2.1100
	BIC	-1.4478	-0.8298	-1.0054	**-0.9533**	-0.2685	-0.4999	1.6566	**1.8081**	**2.1462**
M2	**AIC**	-1.4970	-0.8876	-1.0595	-0.9743	-0.3660	-0.5702	1.5592	1.7987	2.1128
	BIC	-1.4519	-0.8425	-1.0144	-0.9382	-0.3209	-0.5250	1.5973	1.8348	2.1670
M3	**AIC**	-1.4945	-0.8871	-1.0568	-0.9733	-0.3586	-0.5699	1.5502	1.7987	2.1164
	BIC	-1.4494	-0.8420	-1.0117	-0.9373	-0.3134	-0.5248	1.5953	1.8348	2.1705
M4	**AIC**	-1.4974	-0.8898	-1.0587	-0.9716	-0.3682	-0.5709	1.5453	1.8030	2.1169
	BIC	-1.4433	-0.8357	-1.0046	-0.9264	-0.3141	-0.5168	1.5994	1.8481	2.1801
M5	**AIC**	-1.4850	-0.8742	-1.0447	-0.9723	-0.3394	-0.5539	1.5595	**1.7893**	2.1100
	BIC	-1.4489	-0.8381	-1.0086	-0.9453	-0.3033	-0.5178	1.5956	1.8164	2.1462
MX	**AIC**	**-1.5039**	**-0.8970**	**-1.0798**	**-0.9804**	-0.4023	-0.5913	**1.5321**	1.7901	2.1031
	BIC	**-1.4497**	**-0.8429**	**-1.0257**	-0.9263	-0.3391	-0.5281	**1.5953**	1.8081	2.1482
MXR	**AIC**	-1.5000	-0.8923	-1.0612	-0.9778	**-0.4027**	**-0.5938**	1.5414	1.7944	**2.1031**
	BIC	-1.4460	-0.8382	-1.0070	-0.9236	**-0.3395**	**-0.5309**	1.5956	1.8215	2.1482
Panel B: Conditionally heteroskedastic models										
		GL	**NH**	**SH**	**Trpcs**	**NoExt**	**SoExt**	**NoPol**	**SoPol**	**SOl**
M0	**AIC**	-1.4905	-0.8816	-1.0544	-0.9649	-0.3593	-0.5690	1.5524	1.8028	2.1207
	BIC	-1.4364	-0.8274	-1.0002	-0.9198	-0.3051	-0.5148	1.6066	1.8480	2.1749
M1	**AIC**	-1.4685	-0.8467	-1.0266	-0.9647	-0.2979	-0.5259	1.6389	**1.7911**	2.1183
	BIC	-1.4415	-0.8196	-0.9996	-0.9466	-0.2708	-0.4988	1.6659	**1.8001**	2.1544
M2	**AIC**	-1.4932	-0.8798	-1.0565	-0.9713	-0.3599	-0.5704	1.5600	1.7996	2.1166
	BIC	**-1.4571**	-0.8437	-1.0204	-0.9442	-0.3238	-0.5343	1.5961	1.8267	2.1618
M3	**AIC**	-1.4909	-0.8793	-1.0540	-0.9702	-0.3526	-0.5707	1.5558	1.7996	2.1202
	BIC	-1.4548	-0.8432	-1.0179	-0.9431	-0.3165	-0.5346	1.5919	1.8267	2.1654
M4	**AIC**	-1.4936	-0.8818	-1.0558	-0.9684	-0.3621	-0.5714	1.5514	1.8039	2.1207
	BIC	-1.4484	-0.8367	-1.0107	-0.9323	-0.3170	-0.5263	1.5965	1.8400	2.1749
M5	**AIC**	-1.4867	-0.8755	-1.0496	-0.9659	-0.3506	-0.5666	1.5499	1.7993	2.1183
	BIC	-1.4415	-0.8303	-1.0045	-0.9298	-0.3055	-0.5215	1.5950	1.8355	2.1544
MX	**AIC**	**-1.5000**	**-0.8889**	**-1.0787**	**-0.9869**	-0.3558	-0.5907	**1.5408**	1.7911	2.1068
	BIC	-1.4549	**-0.8438**	**-1.0336**	**-0.9599**	-0.3016	-0.5365	**1.5949**	1.8001	2.1429
MXR	**AIC**	-1.4967	-0.8843	-1.0596	-0.9742	**-0.3958**	**-0.5935**	1.5502	1.7911	**2.1068**
	BIC	-1.4516	-0.8391	-1.0145	-0.9291	**-0.3416**	**-0.5393**	1.5953	1.8001	**2.1429**

The Table reports the Akaike (AIC) and Bayes-Schwartz (BIC) information criteria for the Adaptive-AR and the Adaptive-X-AR models for various parameterizations of the level component. The most general specification for the Adaptive-AR model includes switching intercept, linear time trend and Fourier terms (M0). Its five nested specifications are: the constant mean model (M1), the switching intercept model (M2), the linear time trend model (M3), the linear trend model with switching intercept (M4), and the linear time trend model with Fourier terms (M5). The most general specification for the Adaptive-AR-X model includes switching intercept, radiative forcing and Fourier terms (MX). Its nested specification includes radiative forcing and Fourier terms (MXR). Panel A reports the conditionally homoscedastic models; Panel B reports the conditionally heteroskedastic models. The series investigated are average land and ocean temperature anomalies for the entire globe (GL; 90S-90N) and seven zones, namely the Northern Hemisphere (NH; 0-90N), the Southern Hemisphere (SH; 90S-0), the Tropics (Trpcs; 20S-20N), the Northern Extratropic (NoExt; 20N-90N), the Southern Extratropic (SoExt; 90S-20S), the Northern Polar (NoPol; 60N-90N), the Southern Polar (SoPol; 90S-60S).

Table A4: Adaptive-X-AR-GARCH models; estimation sample 1978(12)-2011(12)

Panel A: MX - Adaptive-X-AR model; Radiative forcing specification plus Bai-Perron break process									
	GL	**NH**	**SH**	**Trpcs**	**NoExt**	**SoExt**	**NoPol**	**SoPol**	**SOI**
c_0	-0.093 (0.037)	-0.115 (0.034)	-0.093 (0.032)	-0.093 (0.072)	-0.513 (0.191)	-0.486 (0.178)	-0.943 (0.340)	-	-
c_1	0.237 (0.051)	0.294 (0.049)	0.217 (0.043)	0.202 (0.095)	0.276 (0.059)	0.089 (0.049)	0.312 (0.102)	-	-
c_2	-	-	-	-	0.289 (0.144)	0.315 (0.132)	0.536 (0.257)	-	-
γ_3	-	-	-	-	-	-	0.188 (0.045)	-	-
γ_5 **or** γ_4 **(*)**	0.082 (0.031)	0.105 (0.033)	-	0.137(*) (0.073)	0.143 (0.030)	0.063 (0.025)	0.193 (0.049)	-	-0.519*) (0.201)
δ_5 **or** δ_3 **(*)**	-	-	0.089 (0.029)	0.109(*) (0.083)	-	-	-	-	-
ϕ_1	0.537 (0.048)	0.452 (0.050)	0.487 (0.048)	0.853 (0.028)	0.324 (0.052)	0.330 (0.046)	0.119 (0.053)	0.317 (0.048)	0.465 (0.061)
ϕ_2	0.254 (0.048)	0.230 (0.051)	0.190 (0.046)	-	0.166 (0.051)	0.118 (0.049)	-	-	0.206 (0.063)
ϕ_3	-	-	-	-	-	-	-	-	0.112 (0.058)
β	0.990 (0.010)	0.990 (0.012)	0.990 (0.012)	0.990 (0.014)	0.990 (0.012)	0.990 (0.011)	0.990 (0.014)	0.990 (0.021)	0.990 (0.022)
α	0.010 (-)	0.010 (-)	0.010 (-)	0.010 (-)	0.010 (-)	0.010 (-)	0.010 (-)	0.010 (-)	0.010 (-)
Specification statistics									
AIC	-1.5215	-0.9072	-1.0678	-0.9508	-0.4130	-0.5658	1.4774	1.7569	2.1171
BIC	-1.4713	-0.8571	-1.0177	-0.9005	-0.3528	-0.5056	1.5376	1.7670	2.1573
$Q(20)$	0.6048	0.8413	0.4616	0.0375	0.8414	0.7296	0.3396	0.1029	0.5740
$Q(20)_2$	0.5219	0.0623	0.6742	0.4486	0.0397	0.7318	0.0264	0.5179	0.0017
BJ	0.1467	0.0527	0.7360	0.0157	0.6470	0.2473	0.0000	0.0289	0.0001
Joint Bias	0.6780	0.7522	0.9136	0.1408	0.2949	0.5145	0.1126	0.8162	0.0725

Panel B: MXR - Adaptive-X-AR model; Radiative forcing specification									
	GL	**NH**	**SH**	**Trpcs**	**NoExt**	**SoExt**	**NoPol**	**SoPol**	**SOI**
c_0	-0.806 (0.231)	-0.939 (0.214)	-0.637 (0.198)	-0.615 (0.422)	-1.287 (0.137)	-0.735 (0.127)	-1.699 (0.234)	-	-
c_2	0.565 (0.156)	0.658 (0.145)	0.448 (0.132)	0.424 (0.282)	0.886 (0.093)	0.509 (0.085)	1.160 (0.156)	-	-
γ_3	-	-	-	-	0.137 (0.027)	0.042 (0.024)	0.256 (0.041)	-	-
γ_5 **or** γ_4 **(*)**	0.083 (0.034)	0.106 (0.037)		0.127(*) (0.075)	0.178 (0.029)	0.073 (0.026)	0.207 (0.051)	-	-0.519*) (0.201)
δ_5 **or** δ_3 **(*)**	-	-	0.063 (0.032)	0.137(*) (0.081)	-	-	-	-	-
ϕ_1	0.556 (0.049)	0.479 (0.050)	0.512 (0.048)	0.859 (0.027)	0.321 (0.052)	0.330 (0.046)	0.151 (0.054)	0.317 (0.048)	0.465 (0.061)
ϕ_2	0.254 (0.049)	0.251 (0.051)	0.207 (0.046)	-	0.159 (0.053)	0.118 (0.050)	-	-	0.206 (0.063)
ϕ_3	-	-	-	-	-		-	-	0.112 (0.058)
β	0.990 (0.022)	0.990 (0.010)	0.990 (0.012)	0.990 (0.013)	0.990 (0.016)	0.990 (0.011)	0.990 (0.014)	0.990 (0.021)	0.990 (0.022)
α	0.010 (-)	0.010 (-)	0.010 (-)	0.010 (-)	0.010 (-)	0.010 (-)	0.010 (-)	0.010 (-)	0.010 (-)
Specification statistics									
AIC	-1.5095	-0.8890	-1.0477	-0.9463	-0.4190	-0.5660	1.4954	1.7569	2.1171
BIC	-1.4594	-0.8388	-0.9975	-0.8961	-0.3588	-0.5058	1.5456	1.7670	2.1573
$Q(20)$	0.6408	0.7842	0.6038	0.0449	0.8448	0.6282	0.3317	0.1029	0.5740
$Q(20)_2$	0.3034	0.0043	0.7530	0.4693	0.0086	0.7267	0.0601	0.5179	0.0017
BJ	0.1940	0.0556	0.6602	0.0071	0.4923	0.2537	0.0000	0.0289	0.0001
Joint Bias	0.4359	0.9402	0.9415	0.0995	0.4128	0.3068	0.0468	0.8162	0.0725

Panel A reports the selected Adaptive-X-AR-GARCH models with radiative forcing control variables plus Bai-Perron step dummy variable (MX). Panel B reports the selected Adaptive-X-AR-GARCH models with radiative forcing control variables only (MXR). *AIC* and *BIC* are the Akaike and Bayes-Schwarz information criteria. $Q(20)$ and $Q(20)_2$ are the Box-Ljung test for serial correlation up to the 20*th* order in the standardized and squared standardized residuals, respectively.

BJ is the Bera-Jarque normality test, Joint Bias is the Engle-Ng joint test for asymmetry in variance, Stability is the joint Nyblom stability test. The series investigated are average land and ocean temperature anomalies for the entire globe (GL; 90S-90N) and seven zones, namely the Northern Hemisphere (NH; 0-90N), the Southern Hemisphere (SH; 90S-0), the Tropics (Trpcs; 20S-20N), the Northern Extratropic (NoExt; 20N-90N), the Southern Extratropic (SoExt; 90S-20S), the Northern Polar (NoPol; 60N-90N), the Southern Polar (SoPol; 90S-60S).

Table A5: Adaptive-X-AR-GARCH models using RF in step function; estimation sample 1978(12)-2016(12)

Panel A: MX - Adaptive-X-AR model; Radiative forcing specification plus Bai-Perron break process									
	GL	**NH**	**SH**	**Trpcs**	**NoExt**	**SoExt**	**NoPol**	**SoPol**	**SOl**
c_0	-0.087 (0.045)	-0.112 (0.045)	-0.107 (0.036)	-0.070 (0.069)	-0.140 (0.033)	-0.072 (0.025)	-0.189 (0.062)	-	-
c_1	0.263 (0.059)	0.323 (0.061)	0.253 (0.048)	0.199 (0.078)	0.391 (0.048)	0.202 (0.032)	0.486 (0.078)	-	-
c_2	-	-	-	-	-	-	-	-	-
γ_4 **or** δ_2 **(*)**	-	-	-	-	0.077(*) (0.031)	-	-0.135 (0.058)	-	-
γ_5 **or** δ_5 **(*)**	0.059 (0.032)	0.058 (0.039)	0.060(*) (0.025)		-	0.045 (0.021)	-0.148 (0.071)	-	-
δ_3	-	-	-	0.090(*) (0.042)	-	-	-	-	-0.243(*) (0.171)
ϕ_1	0.581 (0.048)	0.521 (0.051)	0.519 (0.045)	0.865 (0.024)	0.403 (0.049)	0.358 (0.044)	0.194 (0.057)	0.317 (0.048)	0.464 (0.055)
ϕ_2	0.241 (0.045)	0.231 (0.045)	0.186 (0.043)	-	0.185 (0.046)	0.124 (0.045)	0.086 (0.048)	-	0.206 (0.057)
ϕ_3	-	-	-	-	-	-	-	-	0.117 (0.053)
β	0.990 (0.010)	0.990 (0.012)	0.990 (0.012)	0.990 (0.014)	0.990 (0.012)	0.990 (0.011)	0.990 (0.014)	0.990 (0.021)	0.990 (0.022)
α	0.010 (-)	0.010 (-)	0.010 (-)	0.010 (-)	0.010 (-)	0.010 (-)	0.010 (-)	0.010 (-)	0.010 (-)
Specification statistics									
AIC	-1.5065	-0.8858	-1.0657	-0.9806	-0.3697	-0.5748	1.5423	1.7911	2.1119
BIC	-1.4613	-0.8406	-1.0206	-0.9445	-0.3246	-0.5297	1.5965	1.8003	2.1480
$Q(20)$	0.9716	0.7963	0.5732	0.0130	0.7378	0.7518	0.2231	0.3565	0.3891
$Q(20)_2$	0.6342	0.0853	0.6790	0.4920	0.0700	0.8958	0.0360	0.5623	0.0002
BJ	0.0746	0.0000	0.7937	0.1110	0.1216	0.2595	0.0000	0.1198	0.0286
Joint Bias	0.9295	0.4502	0.9810	0.4781	0.9736	0.8532	0.2190	0.6440	0.0310

Panel B: MXR - Adaptive-X-AR model; Radiative forcing specification									
	GL	**NH**	**SH**	**Trpcs**	**NoExt**	**SoExt**	**NoPol**	**SoPol**	**SOl**
c_0	-0.180 (0.103)	-0.284 (0.084)	-0.226 (0.071)	-0.173 (0.143)	-0.331 (0.067)	-0.209 (0.047)	-0.364 (0.127)	-	-
c_2	0.373 (0.147)	0.526 (0.127)	0.419 (0.102)	0.327 (0.204)	0.612 (0.102)	0.383 (0.067)	0.758 (0.188)	-	-
γ_3 **or** γ_2 **(*)**	-0.093(*) (0.053)	0.062 (0.039)	-	-	0.087 (0.033)	-	-0.186 (0.084)	-	-
γ_5 **or** δ_3 **(*)**	-	-	0.035 (0.027)	0.083(*) (0.044)	-	0.028 (0.022)	-0.129 (0.065)	-	-0.243(*) (0.171)
ϕ_1	0.588 (0.048)	0.519 (0.050)	0.535 (0.045)	0.873 (0.023)	0.420 (0.050)	0.359 (0.044)	0.229 (0.056)	0.317 (0.048)	0.464 (0.055)
ϕ_2	0.243 (0.045)	0.238 (0.046)	0.198 (0.043)	-	0.208 (0.046)	0.127 (0.047)	0.117 (0.047)	-	0.206 (0.057)
ϕ_3	-	-	-	-	-		-	-	0.117 (0.053)
β	0.990 (0.022)	0.990 (0.010)	0.990 (0.012)	0.990 (0.013)	0.990 (0.016)	0.990 (0.011)	0.990 (0.014)	0.990 (0.021)	0.990 (0.022)
α	0.010 (-)	0.010 (-)	0.010 (-)	0.010 (-)	0.010 (-)	0.010 (-)	0.010 (-)	0.010 (-)	0.010 (-)
Specification statistics									
AIC	-1.4949	-0.8750	-1.0519	-0.9768	-0.3554	-0.5747	1.5680	1.7911	2.1119
BIC	-1.4498	-0.8299	-1.0067	-0.9407	-0.3103	-0.5295	1.6221	1.8003	2.1480
$Q(20)$	0.8855	0.7895	0.5632	0.0143	0.8240	0.6310	0.0811	0.3565	0.3891
$Q(20)_2$	0.4816	0.1276	0.7661	0.4759	0.0733	0.9256	0.1120	0.5623	0.0002
BJ	0.1136	0.0000	0.7446	0.1065	0.0331	0.6809	0.0000	0.1198	0.0286
Joint Bias	0.8283	0.4972	0.9058	0.3543	0.7049	0.3131	0.0919	0.6440	0.0310

Panel A reports the selected Adaptive-X-AR-GARCH models with radiative forcing control variables plus Bai-Perron step dummy variable (MX). Panel B reports the selected Adaptive-X-AR-GARCH models with radiative forcing control variables only (MXR). *AIC* and *BIC* are the Akaike and Bayes-Schwarz information criteria. $Q(20)$ and $Q(20)_2$ are the Box-Ljung test for serial correlation up to the 20*th* order in the standardized and squared standardized residuals, respectively.

BJ is the Bera-Jarque normality test, Joint Bias is the Engle-Ng joint test for asymmetry in variance. The series investigated are average land and ocean temperature anomalies for the entire globe (GL; 90S-90N) and seven zones, namely the Northern Hemisphere (NH; 0-90N), the Southern Hemisphere (SH; 90S-0), the Tropics (Trpcs; 20S-20N), the Northern Extratropic (NoExt; 20N-90N), the Southern Extratropic (SoExt; 90S-20S), the Northern Polar (NoPol; 60N-90N), the Southern Polar (SoPol; 90S-60S).

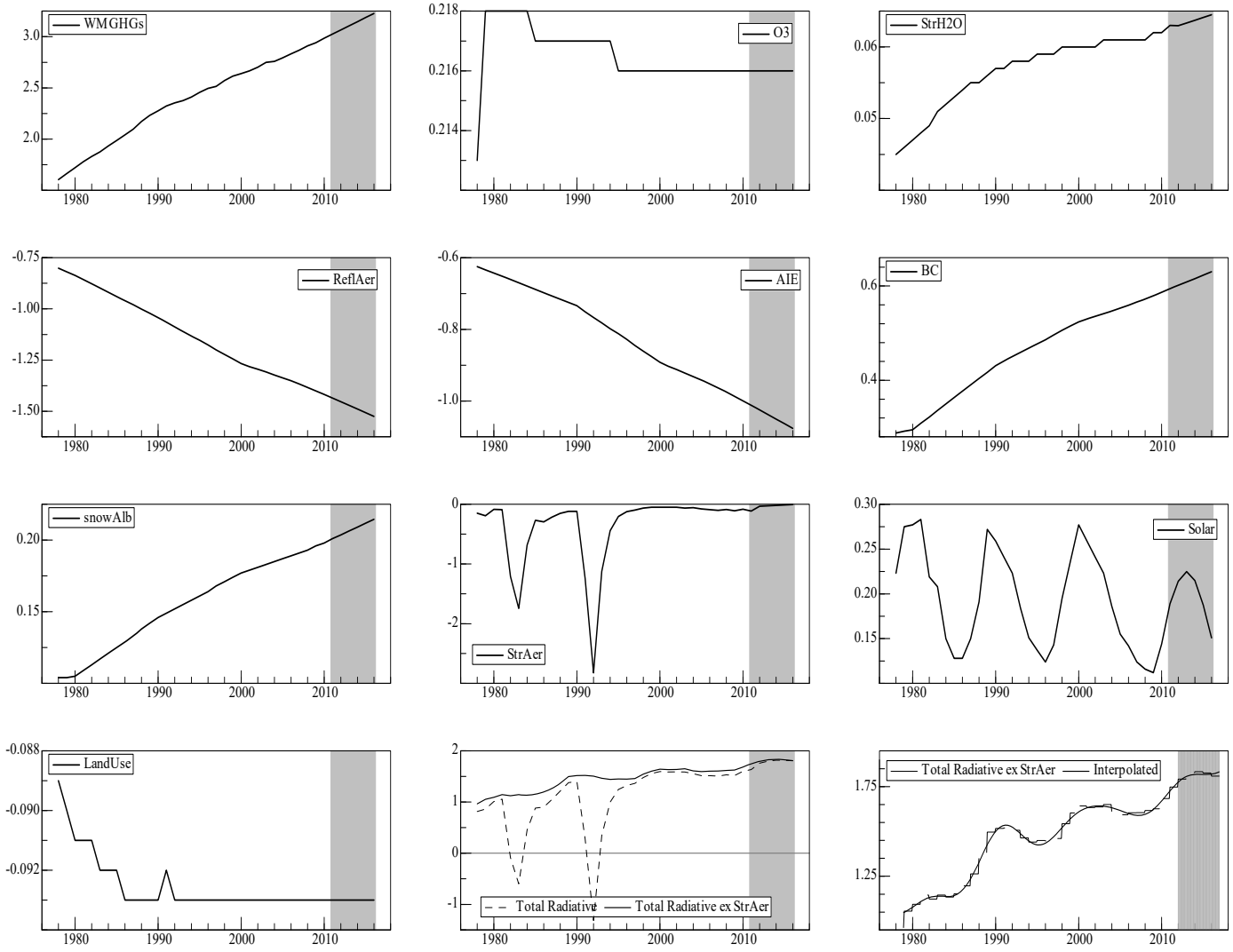

Figure A1: Radiative forcing components and total radiative forcing: actual data, forecasts for 2012-2016 (grey shadow), and monthly interpolated series (Interpolated). Following Hansen et al. (2005), radiative forcing has been decomposed in various categories, i.e., Well-Mixed Greenhouse Gases (WMGG; carbon dioxide (CO_2), methane (NH4), nitrous oxide (N2O) and chlorofluorocarbons (CFCs)), Ozone (O3), Stratospheric Water Vapor (StrH2O), Reflective Tropospheric Aerosols (ReflAer), Tropospheric Aerosol Indirect Effects (AIE), Black Carbon Aerosols (BC), Snow Albedo (snowAlb), Stratospheric Aerosols (StrAer), Solar Irradiance (Solar), Land Use (including irrigation; LandUse). In the plots, Total Radiative corresponds to the sum of the all the reported components; Total Radiative ex StrAer corresponds to the sum of all the reported components with Stratospheric Aerosols (StrAer) omitted.

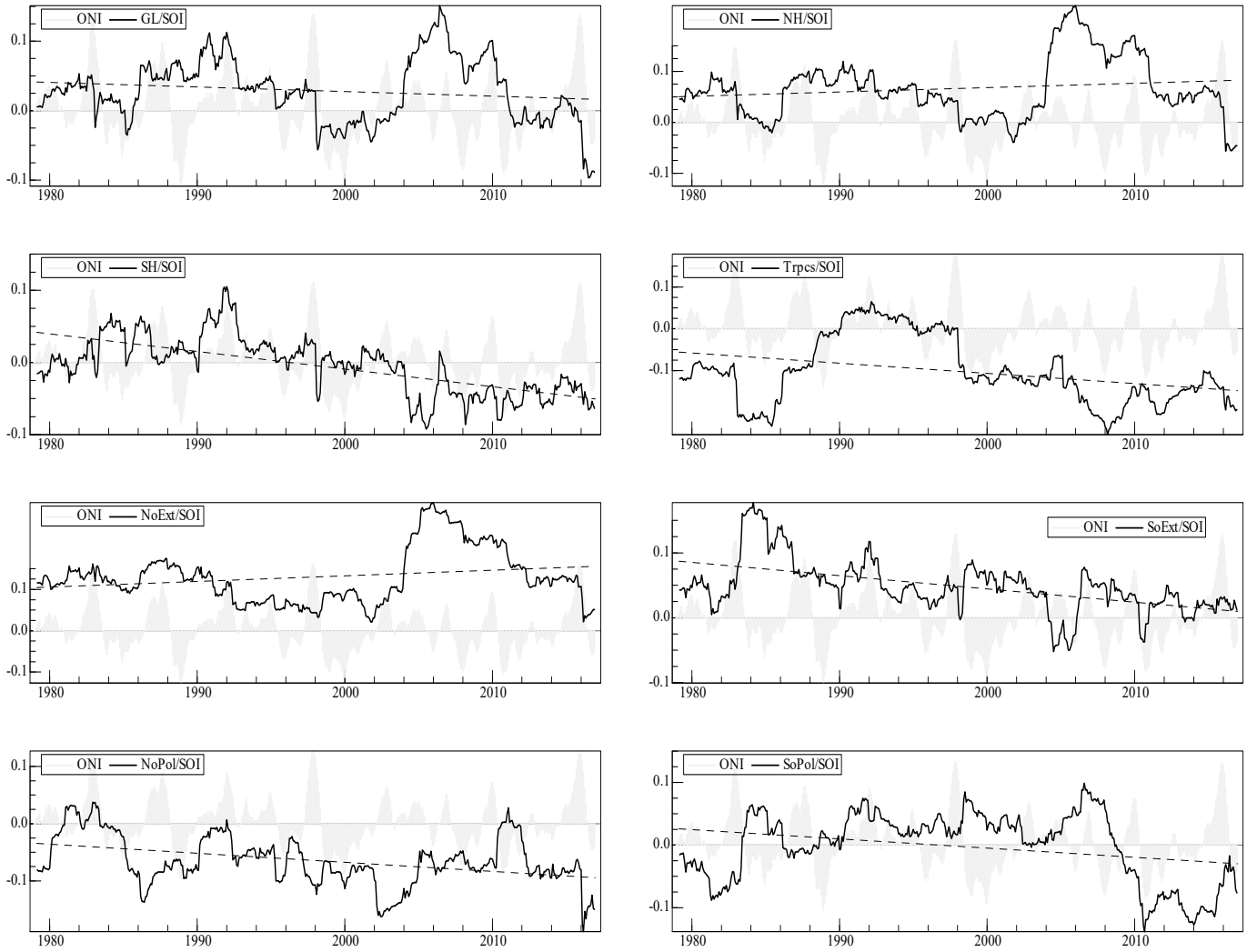

Figure A2: Estimated conditional correlations of the Southern Oscillation Index (SOI) versus various temperature anomalies: the entire globe (GL/SOI), the Northern Hemisphere (NH/SOI), the Southern Hemisphere (SH/SOI), the Tropics (Trpcs/SOI), the Northern Extratropic (NoExt/SOI), the Southern Extratropic (SoExt/SOI), the Northern Polar (NoPol/SOI), the Southern Polar (SoPol/SOI). ONI is the Oceanic Niño Index, scaled to match means and ranges of the various conditional correlations.

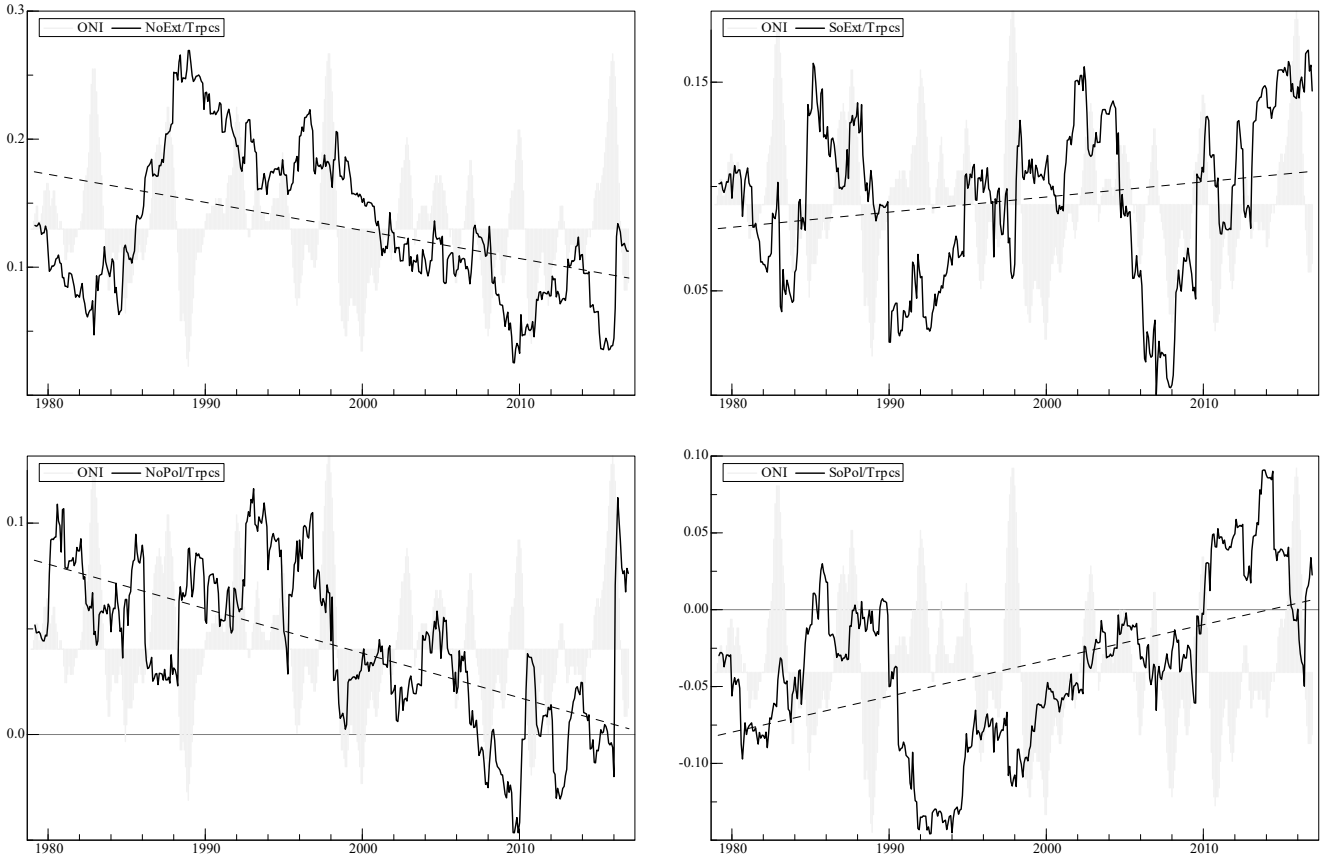

Figure A3: Estimated conditional correlations of Tropics anomaly versus temperature anomalies of various zones: the Northern Extratropic (NoExt/Trpcs), the Southern Extratropic (SoExt/Trpcs), the Northern Polar (NoPol/Trpcs) and the Southern Polar (SoPol/Trpcs). ONI is the Oceanic Niño Index, scaled to match means and ranges of the various conditional correlations.

NOTE DI LAVORO DELLA FONDAZIONE ENI ENRICO MATTEI
Fondazione Eni Enrico Mattei Working Paper Series

Our Working Papers are available on the Internet at the following addresses:
http://www.feem.it/getpage.aspx?id=73&sez=Publications&padre=20&tab=1

NOTE DI LAVORO PUBLISHED IN 2018

1. 2018, CSI Series, Claudio Morana, Giacomo Sbrana, Some Financial Implications of Global Warming: an Empirical Assessment

Fondazione Eni Enrico Mattei
Corso Magenta 63, Milano – Italia

Tel. +39 02.520.36934
Fax. +39.02.520.36946

E-mail: letter@feem.it
www.feem.it

FONDAZIONE ENI
ENRICO MATTEI